An integrated pipeline for building performance analysis

Journal of Building Engineering 75 (2023) 106991

Contents lists available at ScienceDirect

Journal of Building Engineering

journal homepage: www.elsevier.com/locate/jobe

An integrated pipeline for building performance analysis: Daylighting, energy, natural ventilation, and airborne contaminant dispersion

Günsu Merin Abbas [a,b,d,*], Ipek Gursel Dino [a], Mustafa Percin [c]

[a] Dep. of Architecture, Middle East Technical University, Universiteler Mah., Dumlupinar Bulvari, No:1, 06800, Ankara, Turkey
[b] Dep. of Built Environment, Eindhoven University of Technology, Eindhoven, 5600, MB, the Netherlands
[c] Dep. of Aerospace Engineering, METUWIND Experimental Aerodynamics Laboratory, Middle East Technical University, Universiteler Mah, Dumlupinar Bulvari, No:1, 06800, Ankara, Turkey
[d] Dep. of Architecture, TOBB University of Economics and Technology, Söğütözü Cd. No:43, 06510, Ankara, Turkey

ARTICLE INFO

Keywords:
Natural ventilation
Indoor contaminant simulation
Wind tunnel testing
Computational fluid dynamics
Tool development
Building energy performance

ABSTRACT

Early design decisions influence the performance of a building significantly. Yet, computational support for performance assessment during early design is very limited. This research proposes an analysis pipeline for the accurate and comprehensive assessment of building performance by integrating simulation-based analysis tools that perform daylighting, computational fluid dynamics, energy, and contaminant transport simulations, as well as wind tunnel testing that performs velocity and pressure measurements to generate wind pressure coefficients. The pipeline is implemented in three different ways: hybrid, model-based, and empirical workflows. The hybrid workflow combines computational fluid dynamics simulations and wind tunnel testing, while the model-based and empirical workflows utilize computational fluid dynamics simulations and wind tunnel testing, respectively. In the pipeline, computational fluid dynamics is used early on to evaluate a high number of alternatives, leading to the selection of a limited number of good-performing options. Following this, wind tunnel testing is used to "correct" the initial wind pressure coefficient results for increased accuracy. Therefore, a hybrid approach operating with high accuracy that can effectively explore the design search space is needed. The pipeline is tested on a hypothetical office building with different shading device configurations. The coupling of computational and physical testing methods in a hybrid workflow significantly enhanced the accuracy of airflow-related data, which is underestimated by 15.4% using the model-based workflow. Moreover, the hybrid workflow managed the complexity of the design search space by the assessment and elimination of different design alternatives by the stepwise simulation workflow. The inclusion of shading devices also improved the accuracy of airflow-related data. If the shading devices had not been modeled for the simulations and had not been tested, the results would have overestimated the ventilation rate by 85% and underestimated the ventilation rate by 1.4%, respectively. The study's contribution is significant as it proposes a pipeline for a more accurate and comprehensive assessment of building performance, which can inform design decisions and improve the overall building's performance.

* Corresponding author.
E-mail addresses: g.m.abbas@tue.nl (G.M. Abbas), ipekg@metu.edu.tr (I. Gursel Dino), mpercin@metu.edu.tr (M. Percin).

https://doi.org/10.1016/j.jobe.2023.106991
Received 31 March 2023; Received in revised form 29 May 2023; Accepted 31 May 2023
Available online 2 June 2023

Nomenclature

Variables

ρ_{air}	[kg/m^3] Air density
ρ_{eff}	[g/cm^3] Effective particle density
CCL_{BR}	[#/m^3] Contaminant concentration level at the breathing zone
CCL_{total}	[#/m^3] Total contaminant concentration level
C_p	- Wind pressure coefficient
D_{mean}	[nm] Mean particle diameter
R_{gen}	[#/h] Contaminant generation rate
R_{inh}	[m^3/h] Inhalation rate
T_i	[°C] Indoor air temperature
T_o	[°C] Outdoor air temperature
t_{dis}	[HH: MM] Time of discharge
t_{inf}	[HH:MM] Time of infection
VP_{inh}	[#/m3] Inhaled virus particles
U_∞	[m/s] Free-stream wind speed
Q_{vent}	[W] Ventilation sensible heat loss

Acronyms

ACH	Air change per hour
AFN	Airflow network
BPS	Building performance simulation
BR	Blockage ratio
BZ	Breathing zone
CCL	Contaminant concentration level
CD	Computational domain
CFD	Computational fluid dynamics
DGP	Daylighting glare probability
DLA	Daylighting autonomy
IAQ	Indoor air quality
MAE	Mean absolute error
MAPE	Mean absolute percent error
NV	Natural ventilation
PIV	Particle image velocimetry
PR	Perforation ratio
p	Pressure
SC	Scenario category
SD	Shading depth
SHGC	Solar heat gain coefficient
UDI	Useful daylight illuminance
VP	Virus particles
WPP	Wind pressure profiles
WTT	Wind tunnel testing
WWR	Window-to-wall ratio

1. Introduction

Natural ventilation (NV) is important for ensuring healthy and comfortable indoors for building occupants. NV improves indoor air quality (IAQ) and occupants' well-being by replacing contaminated and warm air with fresh air [1]. Poor indoor conditions due to insufficient ventilation may also trigger health problems such as asthma, allergy, breathing problems and airborne virus transmission risks such as COVID-19, SARS and MERS (twice to five times high as compared to outdoors) [2,3]. NV improves thermal comfort by passively cooling the building, resulting in reduced energy demand, HVAC dependency and carbon emissions [4–6]. As NV is related to many factors, including energy demand, indoor air contamination and occupants' well-being, integrated and systematic analysis approaches are essential to satisfy all performance objectives. One of the significant aims of these approaches has been to develop holistic and hybrid strategies to satisfy multiple performance targets [7,8]. Such integrated approaches necessitate the knowledge and expertise of various disciplines and, therefore, should combine multiple evaluation methods and tools [9,10]. Buiding performance simulation (BPS) is integral to these approaches due to its capacity in quantitatively evaluating distinct performance parameters

related to energy use and indoor environmental conditions [11].

In existing studies, energy performance is evaluated in combination with daylight illumination [12–15], visual comfort [16,17] and thermal comfort [18,19]. NV is evaluated in the context of energy performance [5,20–24], thermal comfort and indoor air quality [25–33]. However, NV has not so far been considered as part of an integrated assessment of daylighting, energy performance and indoor air contamination in the literature. This research addresses the need for a combined analysis of these performance measures.

1.1. Existing studies on NV and indoor air contamination

Previous research has shown that the physical conditions in the built environment can be instrumentalized to control NV and reduce the airborne contamination hazard [34–38]. Indoor microclimate conditions (i.e., air temperature, humidity, draft) also directly affect ventilation and the contaminant dispersion behavior, which are also related to the physical conditions of the built environment [39–42]. Previous ventilation and contaminant studies dominantly focus on the role of mechanical ventilation [43–48]. However, the impact of NV on indoor air contamination remains limited in the literature.

The calculation of actual microclimatic data necessitates wind pressure coefficient (C_p) values [49] with high accuracy. C_p is a non-dimensional parameter indicating the wind-driven pressures at particular points in the geometry relative to the free-stream dynamic pressure, which is particularly crucial for modeling NV to predict indoor microclimate accurately [59]. Computational fluid dynamics (CFD) simulations or wind tunnel testing (WTT) are widely used to simulate fluid-flow behavior and obtain C_p values [6]. CFD simulations, although high in computational cost, can help the exploration of a large number of design alternatives. WTT, on the other hand, is laborious and expensive due to the physical modeling and wind tunnel infrastructure it requires. Therefore, the solution space that WTT can analyze is significantly smaller than that of CFD. Nevertheless, WTT is considered the most reliable method to quantify airflow behavior [50,51].

Indoor contaminant assessment also necessitates accurate microclimate data in relation to spatial variation. In the literature, there are various contaminant assessment methods, including the Wells-Riley model [47,52–54], the Monte-Carlo method [55–59] and dose-response models [60–62]. These methods (i) assume contaminant concentration as constant and steady and (ii) neglect spatial variations of the contaminant dispersion [63]. However, actual contaminant dispersion is often non-uniform, and indoor environmental conditions considerably impact contaminant distribution, transportation, dilution and removal [64]. Therefore, contaminant simulations appear to be a viable alternative to the abovementioned methods as they model accurate microclimate and spatial variations.

For the accurate calculation of ventilation and the microclimatic data, the impact of auxiliary façade components such as shading devices on building performance must also be considered. Shading devices are widely used, particularly in office buildings, for effective solar control. They also have a considerable effect on airflow behavior since they define inlet and outlet characteristics. Existing literature largely focuses on the optimization of daylighting and thermal performance of shadings [65]. There are also a number of studies that evaluate he impact of shading devices on NV either in isolation [66–68] or within a limited scope (i.e., only thermal performance) [69,70]. However, the combined impact of shading elements on energy, daylighting and NV-related parameters remain neglected in the literature. Analysis approaches should take into account the influence of shading devices on NV-related performance measures in combination with energy and daylighting parameters.

1.2. Aim of the study

This research problematizes the lack of integrated assessment strategies supporting the evaluation of NV, contamination, energy and daylighting performance. Particularly, disregarding NV and airflow data runs the risk of reducing the level of accuracy of all performance measures. CFD tools and WTT, the two alternative methods that can be used to calculate airflow, have different disadvantages regarding low levels of accuracy, required time and monetary cost. Therefore, a hybrid approach operating with high accuracy that can effectively explore the design search space is needed. In this respect, this study aims to develop an integrated pipeline that supports the analysis of NV and contaminant-related building performance in addition to daylighting illumination and energy use.

The pipeline successively couples simulation tools (daylighting, energy, contaminant simulations) to calculate performance objectives. CFD simulations and physical testing are integrated into this pipeline to account for NV-related airflow effects. In the pipeline, CFD is used early on to evaluate a high number of alternatives, leading to the selection of a limited number of good-performing options. Following this, WTT is used to "correct" the initial C_p results for increased accuracy.

The pipeline is tested using a hypothetical office building with different shading device configurations. We implement the pipeline in three ways. The first workflow combined CFD and WTT, as explained above. The second and third workflows utilize only CFD and WTT, respectively. The separate implementation of these workflows allows us to present a comparative analysis between the analysis results and eventually provide insight into the benefits and challenges of the simulation-based and physical testing-based methods.

1.3. Novelty and contribution of the study

The study's contribution is significant as it proposes an integrated pipeline for more accurate and comprehensive assessment of building performance, which can inform design decisions and improve the overall building's performance. Specifically, the contribution of this paper is four-fold.

[1]The developed pipeline integrates NV (including indoor air contamination), daylighting and energy-related performance measures, which are evaluated concomitantly, that enables multi-criteria performance assessment,

[2]The developed pipeline integrates parametric modeling, simulation-based analysis, and physical testing-based methods. By coupling computational (CFD) and physical testing (WTT) methods, the pipeline can increase the accuracy of airflow-related data. The CFD and WTT have their own advantages and disadvantages. While CFD analysis is cost-effective and fast, it can have limited accuracy due to the many assumptions it requires during modeling. WTT, on the other hand, is generally regarded as more accurate than CFD, but its physical test setup is expensive and time-consuming. Nevertheless, with the developed pipeline CFD and WTT are combined to overcome the disadvantages of using either method alone, such as low accuracy or preparation of the physical test set up,

[3]Practical implications of the pipeline include managing design alternatives and simulation workload, reducing the design search space to a limited number of alternatives. The pipeline employs a hybrid approach that uses CFD and WTT at different stages to calculate airflow behavior accurately and effectively explore the design search space. The hybrid workflow can be used first to reduce the number of design alternatives, followed by physical testing for a few good-performing design alternatives. The targeted high accuracy levels and the physical/computational cost of analysis can be undertaken for mission-critical buildings. For relatively low-risk projects with limited time and budget, the accuracy of CFD testing may suffice and the pipeline can be implemented without WTT. In this respect, the hybrid workflow managed the complexity of the design search space by assessing and eliminating different design alternatives through the stepwise simulation workflow,

[4]Modeling shading devices has led to improved accuracy of airflow-related data and reliable performance analysis results. As we modeled and analyzed the shading devices for an office building, we achieved more precise airflow-related data and, thus, relatively more reliable performance analysis results, as discussed in section 4.3.

The rest of this paper is structured as follows: Section 2 outlines the methodology, the developed pipeline and the performance framework as study metrics. Section 3 presents the case study setup for the pipeline implementation. Section 4 discusses the findings and results of the pipeline implementation. Section 5 presents the main conclusions.

2. Methodology

In this study, we present an integrated analysis pipeline to evaluate the impact of NV on energy performance and indoor air contamination dispersion. The pipeline sequentially integrates several separate simulation-based analysis tools that perform daylighting, CFD, energy and contaminant transport simulations, and WTT as a physical testing method that performs velocity and pressure measurements (Fig. 1). Each tool requires an individual simulation and/or physical model. Daylighting, CFD and energy simulation tools are already integrated into the 3D parametric design environment, enabling the rapid generation of simulation models based on the generated parametric 3D geometry model [71]. The pipeline defines the relationship/data flow/integration between these simulation tools and also integrates contaminant simulations into the workflows.

The pipeline can be utilized in three different workflows regarding the airflow calculation method, more specifically the method of generating and obtaining C_p values: model-based, empirical, and hybrid (Fig. 1). Model-based workflow utilizes only CFD simulation models, empirical workflow utilizes only wind tunnel tests and hybrid workflow utilizes both for airflow calculation. Depending on the expected/targeted accuracy in analysis results, the airflow data (i.e., C_p) can either be generated by CFD, WTT, or both. In the hybrid workflow, C_p is first generated by CFD, then improved by WTT for two reasons. First, CFD can be computationally and time-wise costly to obtain airflow data with high accuracy since the accuracy of the simulations depends on a number of factors (i.e. size of the

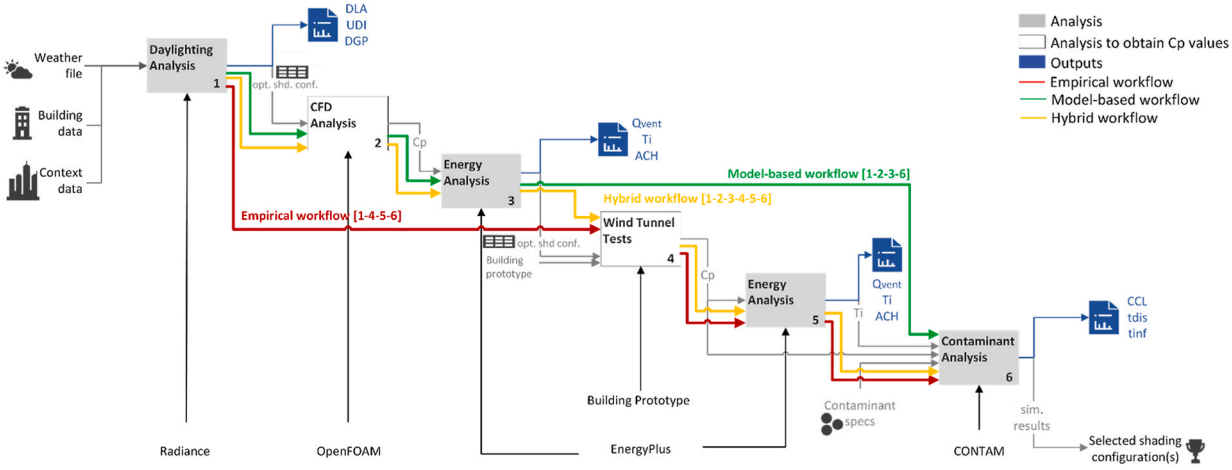

Fig. 1. Pipeline data flow diagram (DLA: daylighting autonomy, UDI: useful daylighting illumination, DGI: daylighting glare probability, C_p: wind pressure coefficient, Q_{vent}: ventilation sensible heat loss/gain, T_i: indoor air temperature, ACH: air change per hour, CCL: contaminant concentration level, t_{dis}: time of contaminant discharge, t_{inf}: time of infection). The results of the outputs in blue will be presented in section 4. (For interpretation of the references to colour in this figure legend, the reader is referred to the Web version of this article.)

computational domain, quality of computational grid, turbulence models, boundary conditions and iterative convergence levels) [72]. Compared to CFD, WTT provides relatively higher accuracy in airflow data [50], yet building several test models for different designs and wind tunnel operation time can be costly. Second, the design search space potentially involves a large number of possible design solutions due to 3D parametric design generation, which should be reduced to decrease the computational and time-wise cost for simulations and physical testing. Therefore, the hybrid workflow first utilizes CFD to reduce the design search space size by relying on CFD-generated C_p and then employs WTT to increase the accuracy of C_p data for the reduced design search space. To demonstrate the impact of the accuracy of the different approaches, this research implemented three workflows separately and performed comparative analyses of their results, as presented in section 4.

The pipeline starts with the generation of a 3D parametric geometrical model and context input (weather and urban geometry

Table 1
Performance measures, outputs and analysis tools.

	Related metrics/Output (s)	Aspect	Quantify (Q) Benchmark (B) Define (D)	Performance target	Tool(s)
Natural Ventilation and Contamination	**Ventilation rate** [ACH]	Fresh Air	**Q:** Fresh air **B:** with IAQ guides **D:** Ventilation adequacy	5 to 15 ACH [73]	EnergyPlus [74] via Honeybee, Ladybug Tools [71], IDF Editor
	Indoor Airflow Velocity [m/s]	Air Velocity	**Q:** Air velocity **B:** with IAQ guides **D:** Indoor draught state	<0.3 m/s [75]	
	Indoor Air Contamination CCL [#/m^3], t_{inf}, t_{dis} [HH:MM]	Contaminated Air	**Q:** Amount of particles Time of discharge **B:** with uncontaminated room conditions **D:** Concentration level	*Contaminant concentration level < infectious dose *Discharge period *Time of infection [34]	NIST CONTAM [76]
Energy	**Indoor Air Temperature** T_i [°C]	Air Temperature	**Q:** Temperature **B:** with IEQ **D:** ΔT, Cooling/Heating impact of natural ventilation	21-23 °C in winter and 22–24 °C in summer for office spaces [75]	EnergyPlus [74] via Honeybee, Ladybug Tools [71], IDF Editor
	Ventilation Sensible Heat Loss Q_{vent} [W]	Cooling	**Q:** Heat loss **B:** ΔQ **D:** Cooling impact of natural ventilation	-	
Daylighting	**Daylighting Autonomy** DLA [%]	Daylight	**Q:** percentage of the time above the illuminance threshold **B:** with IEQ guides **Define:** Daylighting adequacy	For office tasks, 300–500 lux (shallow plan) 500–700 lux (deep plan) [77]	Radiance [78] operationalized via Honeybee, Ladybug Tools [71]
	Useful Daylight Illuminance UDI [%]	Daylight	**Q:** percentage of the time between 200 and 1000 lux **B:** with IEQ guides **D:** Daylighting adequacy	UDI-fell short <100 lux UDI-exceeded>2500 lux 100<UDI-supplementary<500lux 500<UDI-autonomous<2500lux [79]	
	Daylighting Glare Probability DGP [%]	Glare	**Quantify:** Excessive daylight **Benchmark:** with IEQ guides **Define:** Glare probability	Imperceptible (DGP<35%) perceptible (35%<DGP<40%) intolerable (45%<DGP) [80]	
Geometry Model	**3D parametric geometry and simulation models**	-			Rhinoceros 3D [81] and Grasshopper 3D [82]
Intermediary Outputs	**C_p and indoor airflow pattern**	-			CFD: OpenFOAM [83] operationalized via Butterfly, Ladybug Tools [84] WTT (pressure and PIV): Medium-scale suction type wind tunnel

data). Three main analysis steps in the pipeline are daylighting, energy and contaminant transport simulations. Daylighting simulations can be considered as a first stage to reduce design search space that ensures the acceptable IEQ by means of daylighting. The pipeline utilizes CFD and/or WTT as intermediary steps to provide airflow data to energy and contaminant transport simulations. Based on CFD and/or WTT analysis results, C_p values are generated and integrated into the energy analysis to calculate T_i values. Subsequently, in all three workflows, C_p and T_i values are integrated into contaminant transportation simulations to calculate indoor contaminant levels. Based on the results, the performance measures listed in Table 1 are calculated.

In the paper, a number of error analyses are also performed by employing Mean Absolute Error (MAE) and Mean Absolute Percent Error (MAPE) to compare the datasets and to calculate the deviation or discrepancy between the datasets. MAE measures the absolute difference, while MAPE measures the percent difference between the two sets of data [85]. In our study, error analysis is performed to ensure (1) grid quality of CFD analysis, (2) repeatability of WTT measurements, and (3) error between the results generated by the workflows.

Design integration: The pipeline can also be used either for a single design to improve design decisions by obtaining performance feedback or for several design alternatives to be compared/benchmarked to generate/select the final design alternative(s) (Fig. 2). The pipeline is specifically designed to be implemented in several stages that enables the comparison between the design alternatives to reduce the size of the design search space.

2.1. Simulation-based analyses

2.1.1. Daylighting simulations

Daylighting simulations calculate useful daylighting illuminance (UDI), daylighting autonomy (DLA) and daylighting glare probability (DGP). UDI and DLA are calculated by grid-based simulations while DGP is calculated by image-based simulations. Daylighting simulations require a simulation period, an hourly weather file and a sky model based on this hourly weather file.

The daylighting models are generated using the 3D parametric models of an office building. For the grid-based simulations, a test grid with the desired grid resolution is established (Fig. 3a). For the image-based simulations, four viewpoints are identified (Fig. 3b). Two sky models are generated as (1) climate-based sky (exact sky conditions based on the EPW file for the selected period) for UDI and DLA and (2) standard CIE sky (existing sky-defining luminance distributions of commonly simulated sky conditions) for DGP.

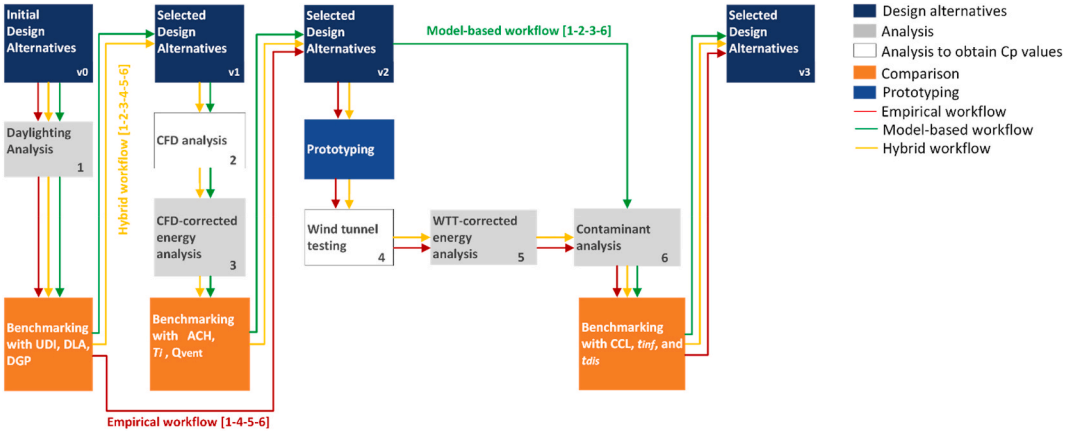

Fig. 2. Pipeline design integration diagram.

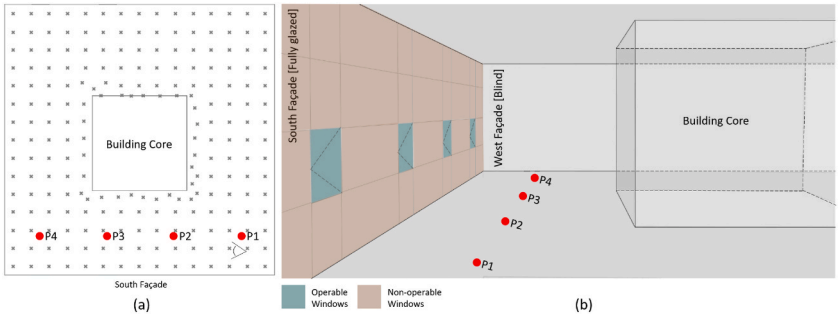

Fig. 3. Daylighting simulation setup (a) an office plan showing the analysis grid and viewpoints for daylighting simulations, and (b) an interior perspective of the office showing the viewpoints and the façade.

2.1.2. CFD simulations

CFD simulations are used to study airflow behavior around objects that are exposed to fluid flows. CFD simulations are based on the numerical solution of the Navier-Stokes equations in a computational domain. The pipeline utilizes CFD simulations to obtain wind pressure data for preliminary ventilation and energy performance assessment. By use of the wind pressure data, C_p values are calculated and used to generate the wind pressure profiles (*WPP*) at each opening as follows [83]:

$$C_p = \frac{p}{0.5\,\rho_{air}\,U_\infty^2} \tag{1}$$

where p is the pressure obtained from CFD test points on the openings, ρ_{air} is the air density (1.225 kg/m^3) and U_∞ is the free-stream wind speed ($U_\infty = 4.3$ m/s).

CFD models are generated using 3D parametric geometry models. The accuracy of CFD simulation results depends on the computational domain (*CD*), quality of analysis grid (meshing and resolution), turbulence models, boundary conditions and iterative convergence levels [72]. *CD* is determined by the best practice guidelines developed by Ref. [86]: the vertical extension and lateral extensions are 5H = 500 m, the leeward extension is 15H = 1500 m and the windward extension is 3H = 300 m, where H is the building height (H = 100 m) (Fig. 4). The openings are defined as flow domains and C_p is calculated in these regions. As a result, the boundary conditions for the contamination simulations are obtained.

Constructing a computational grid (mesh) is the division of the air volume in/around the building geometry into discrete computational cells [9]. The number of cell elements determines the computational cost of CFD simulations and the accuracy of the analysis results [9]. The mesh is generated by *blockMesh* and *snappyHexMesh* utilities, mesh generators of Open FOAM. *blockMesh* constructs parametric meshes with grading and curved edges and decomposes the domain into 3D hexahedral blocks [87]. *snappyHexMesh* constructs 3D meshes of hexahedra and split-hexahedra cells, enabling the iterative refinement of the base mesh [87]. First, *blockMesh* is used to generate a base-level mesh, and then, the mesh is re-constructed and refined by *snappyHexMesh*.

Grid sensitivity analysis is a common practice to determine the mesh quality and the accuracy of the simulation results. A grid convergence study is performed for the baseline case. Three grids are constructed as (1) coarse (1645529 cells), (2) medium (2291234 cells) and (3) fine (2648342 cells). The grid quality is controlled by *snappyHexMesh's global refinement* and *surface feature level* parameters, which are altered for each grid. The resulting grids are checked by *checkMesh*. MAE values are calculated for the scalar velocity and pressure values of the 118 points of the analysis grid (Table 2). The fine mesh setup is selected for further CFD simulations based on the MAE values.

The wind speed and its direction at the inlet of the computational domain are required for the CFD simulations. CFD solutions also require boundary conditions such as inlet/outlet properties or surface roughness [9]. The simulations are performed for a uniform cityscape, which is a terrain that is covered by buildings with similar heights. The aerodynamic roughness is defined as $z_0 = 1$ m. The reference wind speed at $z_{ref} = 50$ m is 4.3 m/s. There are a number of turbulence models, and selecting an appropriate turbulence

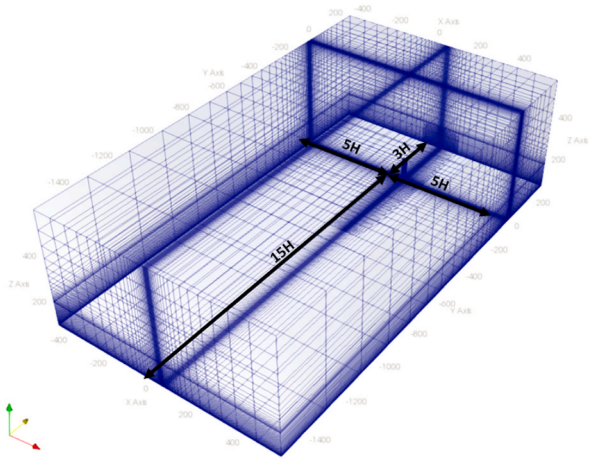

Fig. 4. Flow domain and the selected mesh.

Table 2
MAE for the coarse, medium and fine meshes.

Mesh Comparison	MAE	
	Scalar Velocity [m/s]	Pressure [Pa]
Coarse - Medium	0.4	6.9
Medium - Fine	0.01	0.09

model has a crucial impact on the results [72]. The simulations are performed with Reynolds-Averaged Navier Stokes (RANS) equations and k-ε turbulence model for steady incompressible flows via SIMPLE (Semi-Implicit Method for Pressure Linked Equations) algorithm. Iterative convergence criteria determine the convergence level of the results. In order to achieve tightly converged results, the convergence level is set to 1E-06 for all residuals, as established in the best practice guideline by Franke et al. (2011) [86]. The simulations are performed for four cardinal directions. Finally, C_p values for the cardinal directions are calculated by *Eqn* (1) and integrated into the energy simulations.

2.1.3. Energy simulations

Energy models are generated using the 3D parametric geometry models. Opaque and transparent surface materials are defined as mentioned in section 3.1. Weather data is obtained from the EPW file. Internal loads (people, lighting, and equipment) are defined using the pre-defined EnergyPlus schedules for an open office. The original modeling environment, Ladybug tools [71], is built upon the OpenStudio SDK [88], in which Airflow Network (AFN) module is not yet implemented [89]. AFN is a crucial component of the energy model, which simulates the performance of an air distribution system and supply/return leaks, airflow-induced thermal buoyancy and calculates multizone airflow induced by wind and HVAC systems [90]. In EnergyPlus, there are two possible representations for NV: 'Wind and Stack Area' and AFN. AFN-integrated energy simulations are more accurate as they can incorporate actual C_p values in the calculations. Accordingly, AFN is used to calculate the transient thermal conditions affected by the airflow distribution through NV. Therefore, energy analyses are performed in two stages (Fig. 5). The first energy model is built using the parametric 3D modeling environment, addressed as the "raw energy model" in this study. Following, an IDF file is generated by Honeybee [71] from the raw energy model, which is then corrected by integrating C_p values calculated either by CFD or WTT to AFN using the *IDF Editor*. Thus, the CFD-corrected and WTT-corrected energy models are built. As a result, hourly T_i values are obtained, which are then averaged for the analysis period and used in contaminant analysis.

The results of CFD and initial energy simulations can guide designers sufficiently in the selection of design alternatives for preliminary design stages. Nevertheless, performing CFD simulations depend on a wide range of parameters and often require high computational power and domain expertise, which brings a trade-off between accuracy and complexity [91]. In this respect, it is required to validate and verify CFD simulations with experimental data obtained from WTT or in-field measurements to improve the solution accuracy [50,91], which is particularly critical for the accurate calculation of the actual indoor microclimatic conditions. Therefore, the pipeline adopts a hybrid approach in which CFD simulations are only used for preliminary design feedback whereas wind tunnel measurements are employed to obtain accurate C_p.

2.1.4. Contaminant simulations

Contaminant simulations calculate the transport behavior of airborne particles. So far, the existing contaminant simulations are not coupled yet with 3D parametric design environments. To integrate them into our pipeline, first, the building geometry is required to be modeled in the contaminant analysis tool. Accordingly, a building geometry is generated in the 2D CONTAM SketchPad. Contaminant simulations also require occupancy schedules and weather data. A weather file is needed in WTH format, which can be converted from EPW files using CONTAM Weather File Creator online tool [92]. The transient outdoor air temperature values (T_o) are extracted from the EPW-converted WTH weather file. Contaminant simulations require a contaminant model consisting of contaminant specifications such as molecular weight, particle diameter and effective density, defining the particle's transportation behavior [93]. The contaminant specifications are used as input in CONTAM, as mentioned in section 3. CONTAM constant-coefficient contaminant model is used, which also necessitates contaminant generation and removal rates. Contaminant generation rate (R_{gen}) is a measure of the virus particles emitted by a contaminant source and introduced into space [76]. The removal rate is a measure of the virus particles that the contaminant is deposed from the space [76]. In this study, R_{gen} for COVID-19 is determined based on the empirical research of [94], where the average R_{gen} is 35,366 aerosol virus particles per hour. CONTAM constant-coefficient contaminant model calculates the removal rate during the simulations [95].

CONTAM performs CFD analyses using CFD0 (CFD zero-turbulence model link) to calculate the indoor contaminant concentrations based on the iterative exchange of the boundary conditions [96]. CONTAM-CFD0 link couples a CFD zone and CONTAM AFN for the

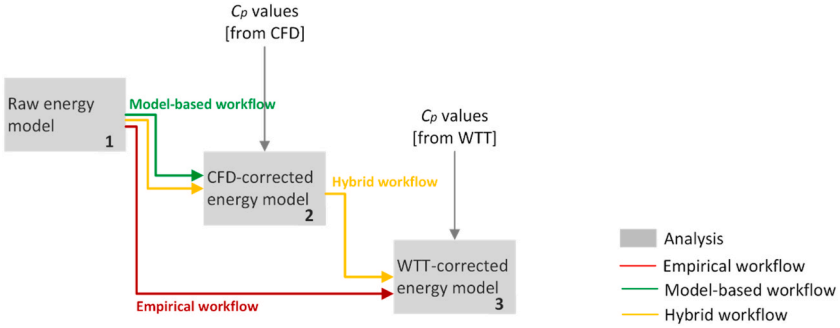

Fig. 5. Energy models.

contaminant transport simulations [96]. Once the required data is provided, C_p values on the openings and flow rates are obtained for the CFD zone. CFD0 calculates airflow behavior and provides feedback to CONTAM (Wang et al., 2010). For contaminant simulations, C_p values are acquired from the CFD in model-based workflow and from the wind tunnel tests in empirical and hybrid workflows.

Contaminant simulations calculate the number of virus particles (*VP*) on user-defined test points in the room. First, contaminant concentration level (CCL) values are calculated as a mass fraction [kg/kg] and converted to the number of particles per unit volume [#/m^3] by *Eqn (2)* [76]:

$$\#/_{m^3} = \frac{kg/_{kg}}{\frac{\rho_{eff}}{\rho_{air}} \frac{1}{6} \pi D_{mean}^3} \tag{2}$$

where ρ_{air} is the density of air, ρ_{eff} is the effective particle density and D_{mean} is the mean particle diameter. CCL values for the test points are calculated by the average integration function in Tecplot 360 EX [97]. Area-weighted average integration calculates the sum of the selected parameter of each test point in the zone or specified subset [97].

CCL values are calculated as follows.

(1) **The room (CCL_{total}):** CCL_{total} is calculated for the whole room by averaging the timestep *CCL* (CCL_t) values during the simulation period:

$$CCL_{total} = \frac{\sum_{i=1}^{m} CCL_t}{m} \tag{3}$$

where CCL_t is the value calculated by the average integration of the whole room, i is the timestep and m is the index of the final timestep.

(2) **Breathing zone in the room (CCL_{BR}):** CCL_{BR} is calculated for the data points (P) between h = 1.20 m and h = 1.80 m height levels.

$$CCL_{BR} = \frac{\sum_{i=1}^{m} CCL_{brt}}{m} \tag{4}$$

where CCL_{brt} is the value calculated by the average integration of the breathing zone in the room, i is the timestep and m is the index of the final timestep.

Infection time (t_{inf}) is the amount of time between the contaminant source's entry into the room and a selected individual's successful infection due to her/his exposure to airborne infectious pathogens. Three parameters are considered to calculate t_{inf}: (i) VP_{inh} is the number of inhaled *VP* [#/m^3] during the occupancy period, (ii) the air exchange volume of the occupant and (iii) the infectious dose of the bio-contaminant. The inhalation rate (R_{inh}) is the measure of the inhaled-exhaled air volume, which depends on occupants' metabolic rate, activity level and activity duration [98]. The infectious dose is the number of *VP* required for successful infection. t_{inf} is calculated as follows:

$$VP_{inh} = \sum_{i=0}^{n} VP_i . R_{inh} \tag{5}$$

$$t_{inf,P} = t_{CE} + t_i \tag{6}$$

where R_{inh} [m^3/h] is the inhalation rate of the occupant, VP_{inh} is the number of *VP* [#] inhaled by the occupant, i is the timestep (hourly), VP_i is the number of *VP* for the selected timestep for the selected data point, $t_{inf,p}$ is the time that the occupant (located at point p) is successfully infected, t_{CE} is the time that the contaminant enters the room and t_i is the amount of time after which VP_{inh} is higher than the infectious dose. The discharge period (t_{dis}) is the time required to discharge the room from the contaminant. t_{dis} is calculated as the time between the contaminant source leaving the room and the complete discharge of the contaminant.

2.2. Model testing

WTT are generally low-speed experimental procedures based on an airflow acting towards scaled building models [9]. In the pipeline, velocity and pressure (internal and surface pressure) measurements are performed to explore the impact of shading devices on indoor (*Pi*) and façade pressure values (P_f), and airflow behavior and indoor airflow velocity.

Pressure tests: Pressure tests are conducted to obtain the wall pressure values on the model surfaces to calculate wind pressure coefficients for the energy and contaminant analyses. Several flexible tubes are mounted on the model surfaces and connected to the pressure scanners for pressure measurements. As a result, C_p values are calculated and used to generate the wind pressure profiles (*WPP*) at each opening as follows [51]:

$$C_p = \frac{p_\times - p_0}{q_\infty} \quad q_\infty = \frac{\rho . U_\infty^2}{2} \tag{7}$$

where $p_\times$ is the pressure derived from a test point on the building façade, p_0 is the free-stream reference static pressure, q_∞ is the dynamic pressure, ρ is the air density and U_∞ is the free-stream wind speed at the room altitude. C_p values are then integrated into the AFN module of the raw energy model. As a result, the WTT-corrected energy model is generated. Energy analysis calculates the final T_i values of the design alternatives. Then, C_p and T_i values are used in contaminant analysis to calculate CCL, t_{dis} and t_{inf}.

Particle image velocimetry tests (PIV): In this study, two-dimensional two-component (2D2C) Particle Image Velocimetry (PIV) experiments are performed to obtain two-dimensional velocity fields in a measurement plane and visualize indoor airflow behavior. PIV is an optical non-intrusive flow diagnostics method based on measuring the displacements of tracer particles that accurately follow the fluid motion [99,100]. In this measurement technique, seeding particles with diameters on the order of 1.0 μm are introduced into air flows upstream of the test model. The flow is generally illuminated through a monochromatic light source (i.e., laser) in the form of a thin plane (with a thickness on the order of a few milimeters) in 2D PIV applications. A camera records two consecutive images of tracer particles within a short time interval. The recorded images are interrogated in sub-regions known as interrogation windows to get the average displacement of the tracer particles within these small areas. A velocity vector for each interrogation window is then calculated using the obtained displacement vector and the known time interval between the consecutive images.

2.2.1. Model prototyping

The prototyping of the physical model is one of the crucial steps of WTT. Two essential parameters determine the properties of the prototype: (1) wind tunnel dimensions determining the scale of the model and (2) the measurement technique to be used determining the prototyping material (i.e., for PIV measurements, the model should be transparent to allow for optical access to the measurement plane whereas pressure measurements do not have such a requirement). The prototype is expected to be robust and resistant to breakages and prevent air leakage. The blockage ratio (BR) is an important parameter that determines the model scale based on the wind tunnel dimensions. In actual conditions, buildings are located in infinite spaces; however, in WTT, test models are exposed to a wind stream with finite cross-section dimensions, which is essentially the cross-section dimension of a closed test section. Therefore, scaled building models are subjected to a blockage effect, which can be considered as the change in incoming wind speed or dynamic pressure [101]. In order to assess the blockage effect, the BR, which is the ratio of the front face of the building in the flow direction to the cross-section area of the wind tunnel test section [86], is evaluated by:

$$BR = \frac{A_b}{A_t}.100 \tag{8}$$

where A_b is the frontal area of the building in the flow direction and A_t is the cross-sectional area of the wind tunnel test section. Typically, a blockage ratio is expected to be $<$ 5–10% [102]. For higher blockage ratios, a blockage correction is recommended. The blockage correction is calculated as [103]:

$$C_c = C_e.\left(1 - \frac{m.A_b}{A_t}\right) \tag{9}$$

where C_c is the corrected coefficient, C_e is the coefficient values calculated based on the WTT, m is the expansion factor for the wake, A_b is the frontal area of the building in the flow direction and A_t is the cross-sectional area of the wind tunnel. Despite the improvements in WTT results, the blockage correction may not be adequate to avoid overestimating results (i.e., acceleration), particularly in building or urban model tests [104]. Artificial acceleration of the flow may occur at the sides of the model since the lateral walls of the tunnel are close to the model [104]. A directional BR can be followed for blockage correction to prevent this artificial acceleration. The directional BR is the decomposition of the BR into a lateral horizontal and vertical directions, which are suggested to be less than 17%, and calculated as:

$$BR_L = \frac{L_b}{L_t} < 17\% \tag{10}$$

$$BR_H = \frac{H_b}{H_t} < 17\% \tag{11}$$

where L_b is the cross-sectional length of the building, L_t is the cross-sectional length of the tunnel, H_b is the height of the building and H_t is the height of the tunnel [104].

In this study, the building model (with a thickness of 5 mm) and shading devices (with a thickness of 4 mm and 6 mm) are fabricated out of transparent plexiglass separately (Fig. 6). The building model is mounted between the top and bottom walls of the wind tunnel test section to eliminate three-dimensional end effects and perform measurements at the mid-height of the model under uniform inflow conditions. The model scale is determined as 1:100 with the corresponding model dimensions of 16 cm x 16 cm x 100 cm (width x depth x height). The BR and BR_L are both obtained as 16%, and BR_H is obtained as 1%. Since the BR_H and BR_L, are smaller than 17%, blockage correction is not required [104] and blockage correction is not applied to the calculations.

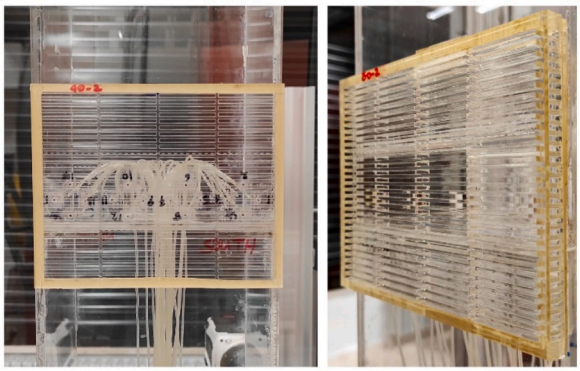

Fig. 6. Fabricated shading devices placed in the tunnel, RÜZGEM METU.

2.2.2. Experimental setup

The experiments are performed in an open-loop suction-type wind tunnel (RÜZGEM C3 wind tunnel) (Fig. 7). It has an eight m-long closed test section with cross-section dimensions of 1 m x 1 m. The test section walls are made of transparent plexiglass to allow for optical access. The maximum free-stream velocity is 25 m/s and the turbulence intensity level is less than 0.5%.

Prior to the actual tests, a short test campaign is run in order to check the repeatability of the measurements. First, the case with the flow at 0° angle is tested twice for each design scenario (SC) (SC-1A to SC-7A). Following, MAE and MAPE for two data sets of each SC are calculated. Each data set consists of 41 measurement points placed on the floor surface of the test section. Average MAE and MAPE are calculated for the pressure values as 0.77 and 4.71%, respectively, which may be regarded as negligible deviations [105] in wind tunnel test results (Table 3).

The wind tunnel experiments are performed under a number of assumptions. First, it is assumed that the test floor of the building at the given height (i.e., between 48th and 52nd meters of the building) will not be subjected to a significant inflow velocity gradient due to the atmospheric boundary layer. Accordingly, the building model is tested under uniform inflow conditions. Second, the dynamic flow similarity is not fully satisfied between the wind tunnel measurements and actual conditions due to the limitations of the wind tunnel assuming the flow to be independent of the Reynolds number and the Froude number in the measurement regime. Although it is expected to observe different characteristics in terms of boundary layer development over the walls and jet flow through the windows as a function of the Reynolds number, the general flow pattern, particularly in the interior space, is assumed to be determined by the flow separations at the sharp corners of the building geometry, which is relatively insensitive to the Reynolds number. On the other hand, since structural vibrations of the building and buoyancy effects are not considered design parameters in the study, the Froude similarity is not applied in the wind tunnel experiments.

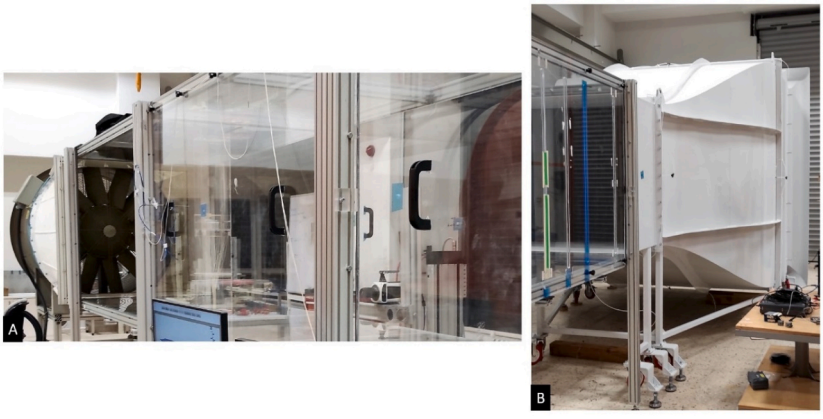

Fig. 7. RÜZGEM C3 wind tunnel: views towards a) the test section, and b) the settling chamber.

Table 3
Repeatability test.

	SC-1A	SC-2A	SC-3A	SC-4A	SC-5A	SC-6A	SC-7A	AVERAGE
MAE [Pa]	1.07	0.31	0.1	0.95	1.15	1.31	0.47	0.77
MAPE [−]	7.12%	2.04%	0.60%	5.71%	6.90%	7.78%	2.80%	4.71%

Pressure Test Setup: Pressure taps should be located on the model to measure wall static pressures in the wind tunnel. For this purpose, 16-gauge (1.63 mm) metal and 1.37 mm flexible capillary tubes are employed. The metal and flexible capillary tubes are shrink-fitted to each other, while the metal tubes are attached to the holes on the model surfaces. The flexible capillary tubes are connected to a 64-channel pressure scanner (Scanivalve MPS 4264) to register pressure values on the pressure taps. 41 and 32 pressure taps are mounted on the interior ground surface and the N-S façades of the model (16 for N, 16 for S), respectively (Fig. 8). The models are tested for four wind directions for each case to obtain C_p data. The models are also tested for four ordinal wind directions, which are diagonal to the model to compare the impact of wind angles on indoor pressure. A step motor is mounted under the test model to change its orientation with respect to the uniform free stream (Fig. 9).

PIV Test Setup: PIV tests are performed for all SC-A (wind direction: North, 0°) and SC-C (wind direction: South, 180°) cases to visualize the indoor airflow. Fig. 10 shows the experimental setup for the PIV measurements, which consists of a Phantom v641 high-speed camera with a Nikon-Nikkor 60 mm lens, a New Solo PIV Nd:YAG laser, a Dantec Dynamics timer box and Dynamic Studio data acquisition and analysis software. The laser is placed on a 3-axis traverse, and the light beam is emitted from the laser along the

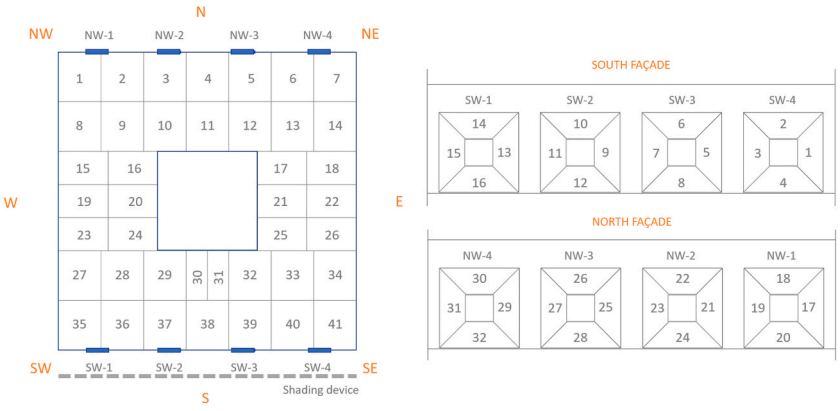

Fig. 8. Pressure tap locations on the model (left: interior, right: façades).

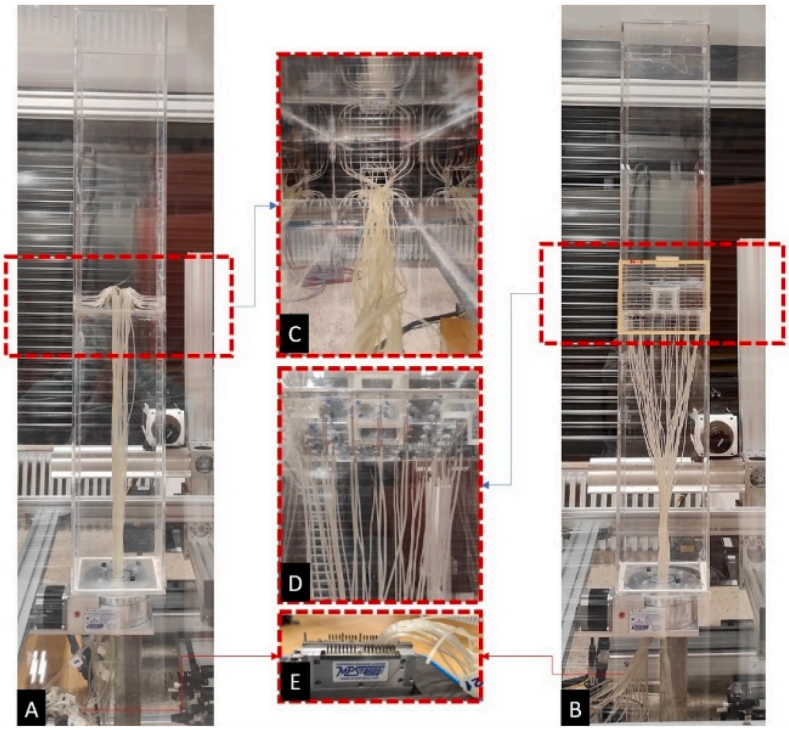

Fig. 9. Experimental setup for the pressure measurements, RÜZGEM METU: a) flexible capillary tubes fixed to the model façades, b) the model with a shading device, c) flexible capillary tubes inside the model, d) flexible capillary tubes fixed to the model floor surface, and e) pressure scanner.

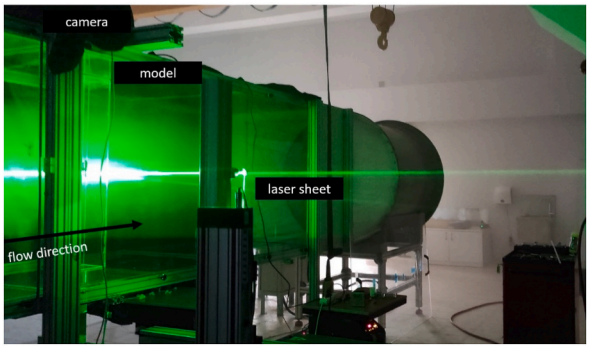

Fig. 10. PIV test setup, RÜZGEM METU.

horizontal section of the building model while the camera is placed on top of the wind tunnel's top wall looking downward through the wind tunnel test section. The incoming 4.3 m/s airflow from the tunnel inlet is seeded with ~ 1 μm diameter particles, which are used as tracer particles. For each case, 1000 double-frame images of tracer particles are recorded by means of the high-speed camera at a recording rate of 10 Hz to ensure converged statistical analysis. The low-pass filtering method is used for the pre-processing of the captured particle/flow images to improve visual quality and remove background noise. The pre-processed images are then cross-correlated using windows of final size 64 × 64 pixels^2 with an overlap factor of 50%, yielding a resultant vector resolution of 3.5 mm. The erroneous vectors are detected and replaced by the use of the universal outlier detection technique [106].

3. Case study setup

The pipeline is implemented for a hypothetical, naturally ventilated open office. The building is located in Ankara, which has a temperate climate suitable for NV [107]. The building has shading devices on the south façade. In this building, the proposed pipeline is used to explore various shading configurations that can satisfy different performance objectives, such as reducing solar heat gains and reducing indoor glare problems while providing adequate natural ventilation.

The following model parameters are considered in the building: local climate and context, spatial configuration, building geometry and façade treatment (based on CTBUH guidelines [107]).

Context: The simulations are performed for a uniform cityscape. The terrain is covered by buildings with similar heights and open spaces.

Local climate: The building is in Ankara, Turkey. Ankara belongs to the Csb climate zone, which has a Mediterranean climate. Ankara receives the northern and north-northeastern winds throughout the year and western-northwestern winds during the warm months. Ankara has a relatively low humidity ratio, which increases natural ventilation potential.

Simulation Period and Weather Data: The simulation period is set to a day of a typical summer week in Ankara as defined in the STAT file (August 20th) between 8:00–18:00. The average dry bulb temperature (25.7 °C), relative humidity (35.3%) and wind speed (4.3 m/s) are calculated as average values from the existing EPW. The transient values in the existing EPW are replaced by the averaged values. Thus, EPW files are generated for four wind directions (0°, 90°, 180°, 270°).

Building: The building has 25 floors and a shallow open-plan layout (15x15x100 m^3 dimensions and 4 m floor height) with a 5x5 m^2 core in the middle (Fig. 11). A mid-rise building is preferred since NV may not be an effective strategy for tall buildings due to

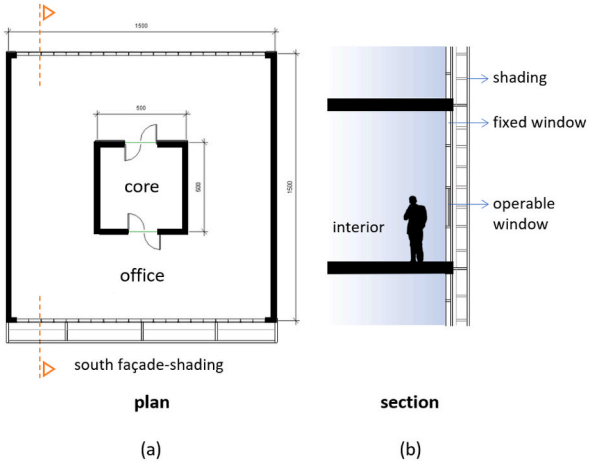

Fig. 11. Building floor plan and section.

unpredictable wind behavior, accelerated wind velocity, wind noise, draft and safety risks at higher altitudes [64]. Moreover, a shallow plan is recommended for better ventilation and daylighting [75]. We only focus on the analysis of the 12th floor of the building (Fig. 12). The indoor surfaces (two slabs and four interior walls) are set to adiabatic surfaces, while four exterior walls are exposed to outdoor conditions. The R-value of the exterior concrete walls is set to 0.30 m^{2}K/W. The U-value of the glazing is set to 1.4 W/m^{2}K. The glazing materials' solar heat gain coefficient (SHGC) is 0.55 and the visual transmittance is 0.78. Window-to-wall ratio (WWR) is $<$12% due to the Turkish Code on Energy Performance of Buildings [108].

Façade Strategy: North and South façades are fully glazed single-skin, and there are four operable windows on the North and South façades each (Fig. 11). The shading devices are located only on the south façade. The single skin façade is based on three layers from inside to outside (1) windows (both operable and fixed), (2) a construction system carrying the shading devices and (3) the shading devices (Fig. 13). There is a 0.40 m gap between the shading devices and the windows for the construction system.

Shading Devices: Six shading device alternatives are designed for the south façade. The perforation ratio (PR) and the shading depth (SD) are determined as the two design parameters. Two PR values (40% and 60%) and three SD values (40 cm, 60 cm and 80 cm)

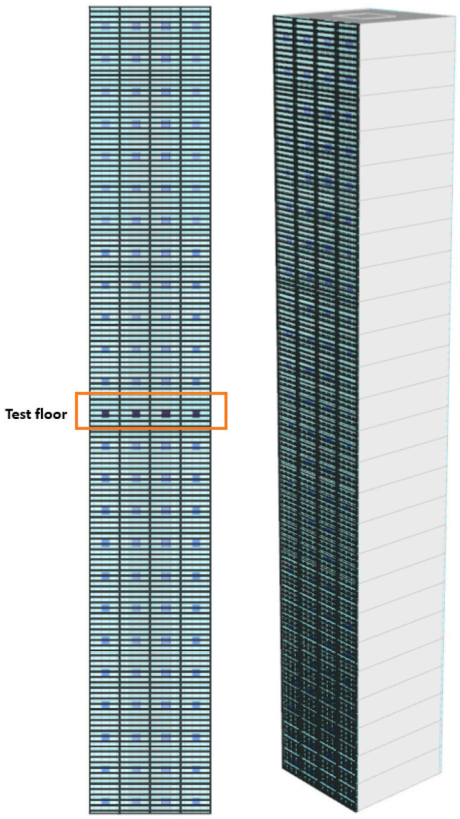

Fig. 12. Test floor and the south elevation.

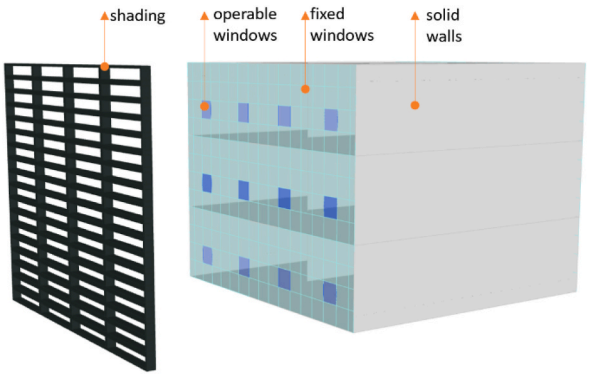

Fig. 13. Façade design strategy.

are defined for the shading devices (Fig. 14).

Occupancy scenario: The building is assumed to be occupied by 0.15 ppl/m^2 between 8:00–18:00. The occupants are engaged in office activities. The activity level is specifically defined to precisely calculate occupants' R_{gen} and R_{inh}. However, it must be noted that the simulation results can vary due to different activity levels that can influence metabolic rates, expiratory activities, contaminant emission and R_{gen} of the occupants.

Contaminant specifications: COVID-19 is selected as the bio-contaminant species. COVID-19's specifications that are required for the contaminant simulations are as follows: the molecular weight is 33797.0 Da (33.79 kg/kmol) [109], the diameter is 100 nm (0.1 μm), which is the average value of the diameter range (between 60 and 140 nm) [110], particle's effective density is set to 1.0 g/cm^3 [93].

Infection scenario: The infected person, shown in Fig. 15, stays in the room between 9:00 and 10:00. The height of the infected person is set to 1.20 m in a sitting position. In the literature, different accounts for the COVID-19 R_{gen} exist for different experimental

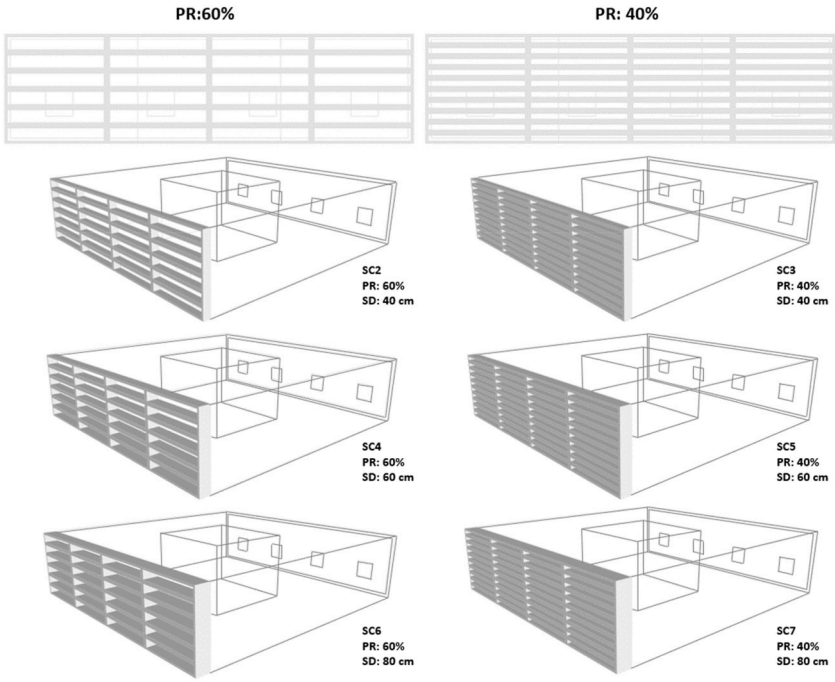

Fig. 14. Shading device alternatives.

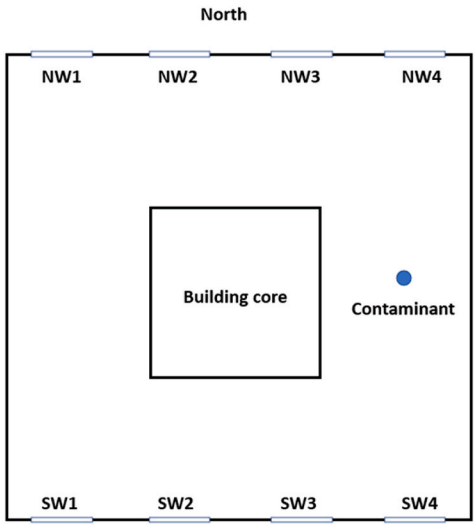

Fig. 15. Contaminant location.

setups. Furthermore, the COVID-19 R_{gen} varies significantly with respect to activities, the infection phase and particle characteristics [111]. In this research, R_{gen} is taken from the study of [94], who analyzed COVID-19 infected breath samples during 30-min of breath sampling [94]. COVID-19 is detected in 40% of the aerosol samples (4 out of 10 participants with a maximum of $10^{4.7}$ and a minimum of $10^{2.8}$ particles per 30 min). The calculated average R_{gen} is 35,366 aerosol virus particles per hour.

Design Scenarios (SC): The pipeline is implemented for seven scenario categories for six shading device configurations and a baseline geometry (Table 4). The baseline scenario category (SC-1) is established for benchmarking, which does not have a shading device. Each scenario category is simulated for four wind directions (0°, 90°, 180° and 270°) to evaluate the impact of the shading configuration concerning wind direction on indoor air. In all scenarios, the office is free-running (no climatization) and naturally ventilated. T_i is calculated separately for each scenario based on the CFD and the WTT-corrected energy analysis and used in the contamination simulations.

4. Analysis results and findings

This section presents the simulation-based and physical testing-based analysis results for model-based, empirical, and hybrid workflows. We focus on the impact of shading device configuration on daylighting, energy, natural ventilation and air contamination measures. We first analyze daylighting simulation results to determine the shading configurations that fulfill the daylighting performance requirements for UDI, DLA and DGP. Following this, we analyze CFD-corrected and WTT-corrected energy simulation results for T_i, Q_{vent} and ACH. We also analyze pressure and PIV experiment results regarding the impact of the shading configuration on indoor airflow behavior (pressure and airflow speed). Finally, we analyze the contaminant simulation results of the shading configurations for CCL, t_{dis} and t_{inf}.

Table 4
Scenario categories and scenarios.

Scenario Categories	Scenarios	PR	SD	Wind Direction
SC-1	SC-1A	-	-	0°
	SC-1B			90°
	SC-1C			180°
	SC-1D			270°
SC-2	SC-2A	60%	40 cm	0°
	SC-2B			90°
	SC-2C			180°
	SC-2D			270°
SC-3	SC-3A	40%	40 cm	0°
	SC-3B			90°
	SC-3C			180°
	SC-3D			270°
SC-4	SC-4A	60%	60 cm	0°
	SC-4B			90°
	SC-4C			180°
	SC-4D			270°
SC-5	SC-5A	40%	60 cm	0°
	SC-5B			90°
	SC-5C			180°
	SC-5D			270°
SC-6	SC-6A	60%	80 cm	0°
	SC-6B			90°
	SC-6C			180°
	SC-6D			270°
SC-7	SC-7A	40%	80 cm	0°
	SC-7B			90°
	SC-7C			180°
	SC-7D			270°

Table 5
Correlation between daylighting performance metrics and shading parameters.

	Glare	DLA	UDI
SD	-0.57	-0.42	-0.43
PR	0.77	0.83	0.72

4.1. Analysis results

4.1.1. Daylighting analysis

Daylighting simulations are only performed for the scenario categories since wind direction does not have an impact on the daylighting results. Therefore, the best-performing design options are selected for CFD and energy simulations. For each SC, the simulation results are inspected both visually and numerically (Fig. 16). SC-3, SC-5, and SC-7 remained below the DLA threshold (50% for office tasks: 300–500 lux), resulting in 39.8%, 37.4%, and 37.2%, respectively. SC-6 also remained below the DLA threshold but showed a higher UDI value. In all SC, DGP values are within the imperceptible glare range. SD and PR considerably influence daylighting performance for both daylight illumination and glare. There is a strong negative correlation (p = -0.57) between SD and glare whereas there is a medium negative correlation between SD and DLA (p = -0.42) and SD and UDI (p = -0.43). There is a strong positive correlation between PR and glare (p = 0.77), PR and DLA (p = 0.83) and PR and UDI (p = 0.72). As a result, if SD increases, glare and daylighting decrease simultaneously. Contrary to this, both glare and daylighting increase with the increase in PR (Table 5).

4.1.2. Energy analysis

Two sets of energy analyses are performed: (i) CFD-corrected energy model and (ii) WTT-corrected energy model. Air change rate (ACH), ventilation-sensible heat loss (Q_{vent}) and indoor air temperature (T_i) are calculated for each scenario (Table 6). The impact of SD and PR on Q_{vent}, T_i and ACH is also evaluated. The correlations are calculated based on the hybrid workflow.

Ventilation-sensible heat loss (Q_{vent}): There is a moderate negative correlation (p = -0.45) between SD and Q_{vent} whereas there is a strong positive correlation (p = 0.88) between PR and Q_{vent}. The wind acting perpendicular to the façade with openings (SC-A and SC-C) increases Q_{vent} by 81.4% on average compared to the wind acting parallel to the façade with openings (SC-B and SC-D). Also, the wind acting upon the façade with shading devices (SC-C) decreases Q_{vent} by 1.53%. As a result, Q_{vent} decreases with the increase in SD whereas Q_{vent} increases with the increase in PR. Moreover, the shading devices reduce ventilation-sensible heat loss when they receive direct airflow.

T_i: There is a moderate negative correlation (p = -0.44) between SD and T_i whereas there is a strong positive correlation (p = 0.84) between PR and T_i. The wind acting perpendicular to the façades with openings (SC-A and SC-C) results in 2.5 °C (9%) on average lower T_i as compared to wind acting parallel to the façades with openings (SC-B and SC-D). There is a negligible difference (0.08%) in T_i values of SC-A and SC-C scenarios.

Air change rate (ACH): There is a moderate negative correlation (p = -0.46) between SD and ACH whereas there is a moderate positive correlation (p = 0.42) between PR and ACH. The wind acting perpendicular to the façades with openings (SC-A and SC-C) increased ACH rate 5.2-fold compared to the wind acting parallel upon the façades with openings (SC-B and SC-D). SC-C (wind acting upon the façade with shading devices) decreased ACH by 1.2% on average compared to the SC-A (wind acting upon the façade

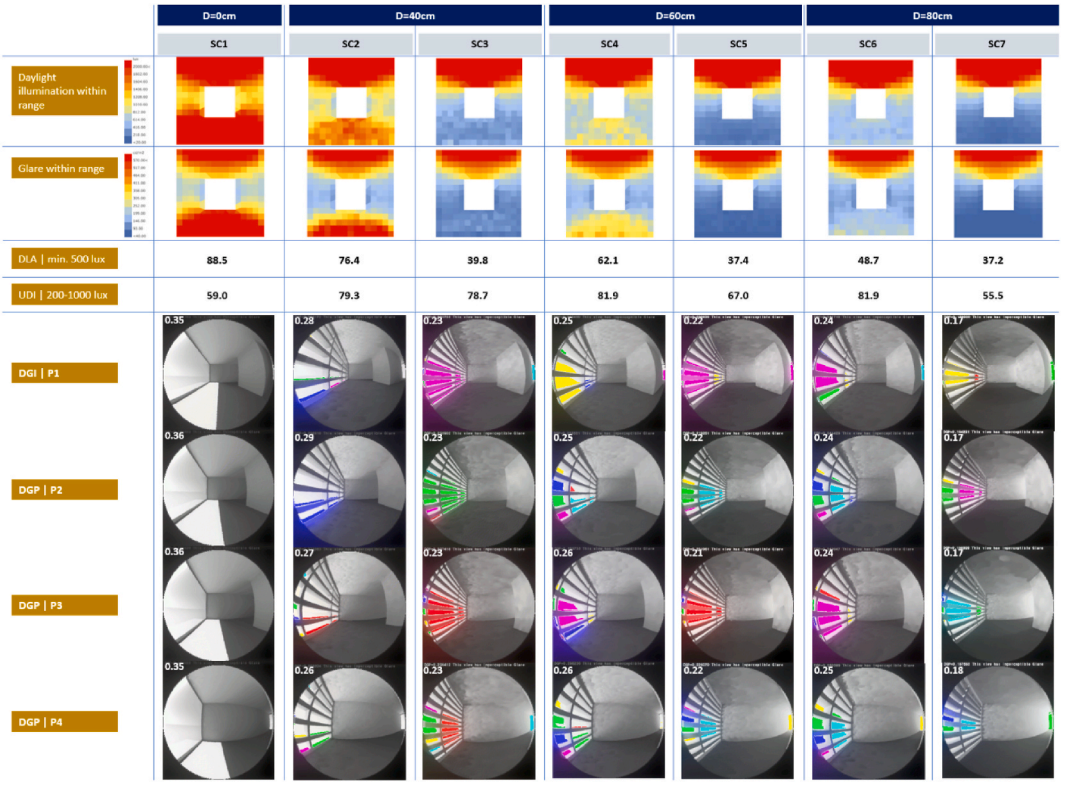

Fig. 16. Daylighting analysis results.

Table 6
Analysis results of the model-based, empirical and hybrid workflow implementation for the scenarios.

Scenario Categories	Scenarios	CFD-corrected energy analysis results [Model-based workflow]			Wind tunnel-corrected energy analysis results [Empirical and hybrid workflow]		
		Average T_i (°C)	Average Ventilation Sensible Heat Loss (W)	Air Change Rate (ACH)	Average T_i (°C)	Average Ventilation Sensible Heat Loss (W)	Air Change Rate (ACH)
SC-1	**SC-1A**	25.7	5620	33	25.1	5593	32
	SC-1B	29.4	3212	6	28.4	3222	6
	SC-1C	25.8	5546	32	25.1	5516	31
	SC-1D	29.4	3249	6	28.4	3261	7
SC-2	**SC-2A**	25.5	3522	33	24.8	3509	32
	SC-2B	28.1	1879	5	27.2	1898	6
	SC-2C	25.5	3449	32	24.8	3466	32
	SC-2D	28.1	1902	6	27.2	1908	6
SC-3	**SC-3A**	25.5	3328	33	24.8	3320	33
	SC-3B	27.9	1756	5	27.0	1774	6
	SC-3C	25.9	2969	16	24.8	3269	32
	SC-3D	27.9	1779	6	27.0	1786	6
SC-4	**SC-4A**	25.5	3446	33	24.8	3438	32
	SC-4B	28.0	1826	5	27.1	1850	6
	SC-4C	25.5	3370	32	24.8	3388	32
	SC-4D	28.0	1855	6	27.1	1863	6
SC-5	**SC-5A**	25.5	3290	33	24.8	3282	32
	SC-5B	27.9	1733	5	27.0	1751	6
	SC-5C	25.9	2933	16	24.8	3231	32
	SC-5D	27.9	1756	6	27.1	1763	6
SC-6	**SC-6A**	25.5	3393	33	24.8	3383	32
	SC-6B	28.0	1794	5	27.1	1818	6
	SC-6C	25.5	3317	32	24.8	3334	32
	SC-6D	28.0	1817	6	27.1	1824	6
SC-7	**SC-7A**	25.5	3264	33	24.8	3246	31
	SC-7B	27.9	1717	5	26.9	1733	6
	SC-7C	25.8	2910	16	24.8	3177	31
	SC-7D	27.9	1740	6	26.9	1744	6

without shading devices).

4.1.3. Wind tunnel test analysis

Pressure *(P)* analysis: C_p data is generated based on the four cardinal wind directions and integrated into the raw energy models. Four ordinal wind directions are also tested to isolate the impact of wind direction on façade and indoor air pressures. The analysis results are investigated to explore the impact of shading devices on indoor pressure values (P_i) and façade pressure values (P_f). The average pressure results are presented in Fig. 17, Figs. 18 and 19 reveal that the airflow direction is considerably influential on pressure values.

Indoor pressure (P_i): SC-C results in the highest P_i, whereas SC-B (90°) and SC-D (270°) result in the lowest P_i. Also, SC-A (0°) and SC-C (180°) result in higher P_i than the airflow from the diagonal angles (45°, 135°, 225° and 315°) (Fig. 17). As a result, airflow acting perpendicular to the façade with openings results in higher P_i than the airflow from the diagonal angles. Airflow from the side angles to the façade with openings results in the lowest P_i. The façades with shading devices exposed to the perpendicular airflow result in higher P_i.

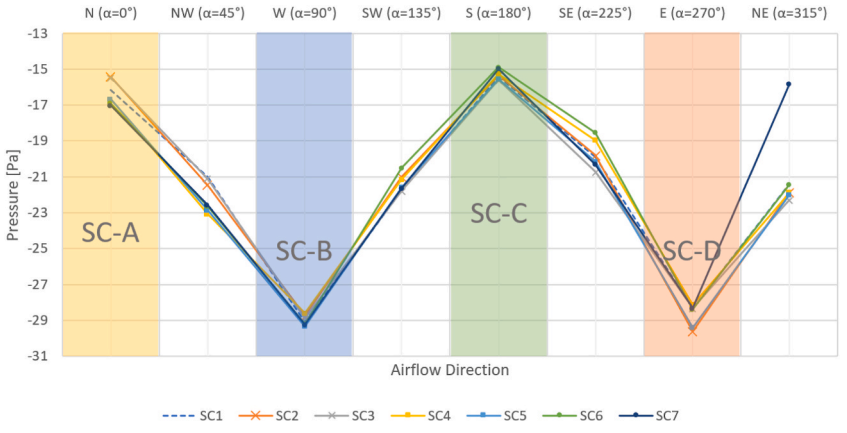

Fig. 17. Indoor surface pressure values.

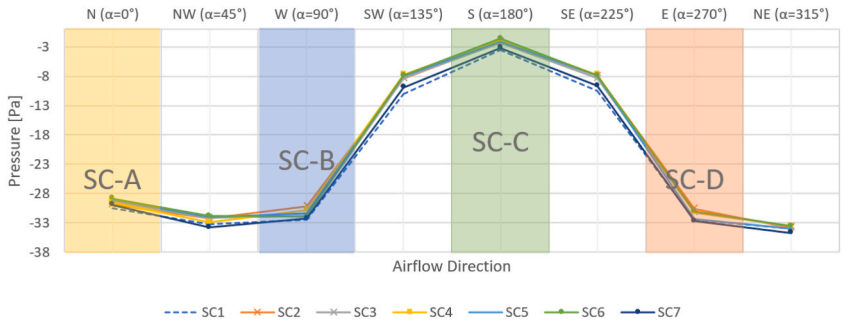

Fig. 18. P_f of the North façade (acquired through WTT).

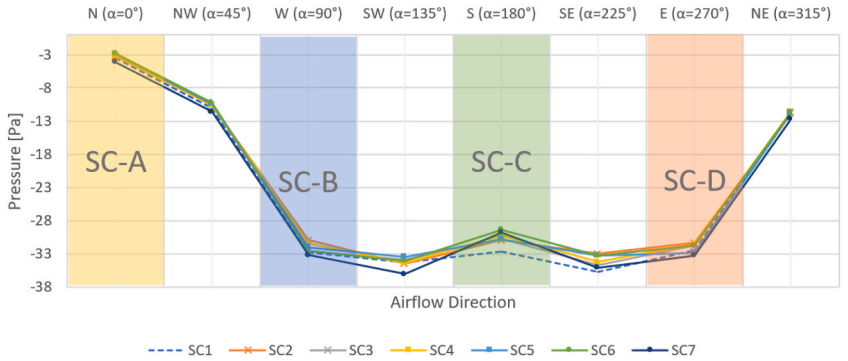

Fig. 19. P_f of the South façade.

The impact of SD and PR on P_i is also inspected. The results suggest that the relationship between both SD and P_i, and PR and P_i are considerably dependent on the airflow direction and the orientation of the façade with shading devices. Table 7 shows that there is a strong inverse correlation between SD and P_i for SC-A (r = -0.95), SC-D (r = -0.62) and airflow from 45° (r = -0.74). Contrary to this, there is both moderate and strong positive correlation between SD and P_i for SC-C (r = 0.81), SC-B (r = 0.43), airflow from 135° (r = 0.35), 225°(r = 0.43) and 315° (r = 0.61). As a result, if airflow directly acts upon the façade with shading devices, P_i increases parallel to SD. Conversely, if airflow acts in the opposite direction, P_i decreases as SD increases. As Table 7 suggests, PR is particularly influential in the scenarios that receive airflow from 90°, 135°, 225° and 180°. As a result, PR is mainly influential in the scenarios where airflow acts directly upon the façade with the shading devices.

Façade pressure (P_f): P_f is investigated only for the North (N) and the South (S) façades. Airflow from 180° to 315° led to the highest and lowest P_f for N, respectively. Similarly, in all scenarios, airflow from 0° to 135° have led to the highest and lowest P_f for S, respectively. The impact of PR and SD on P_f is also inspected. As Table 8 suggests, there is a positive correlation between the PR and P_f of both N and S façades for all directions. Contrarily, there is a negative correlation between the SD and P_f of both N and S façades for most of the airflow directions. For the N façade, PR is relatively more significant as compared to SD whereas for the S façade, SD is particularly influential. As a result, independent of the shading devices, P_f increases as SD decreases for all airflow directions for the S façade. This is due to decreasing losses with decreasing SD, yielding relatively higher pressures on the façade walls. In a building with

Table 7
Correlation between (i) P_i and SD and (ii) P_i and PR.

	[SC-A]		[SC-B]		[SC-C]		[SC-D]	
	0°	45°	90°	135°	180°	225°	270°	315°
SD	-0.95	-0.74	0.43	0.35	0.81	0.43	-0.62	0.61
PR	0.04	-0.13	0.56	0.89	0.41	0.85	0.04	-0.37

Table 8
Correlation between (i) P_f and SD and (ii) P_f and PR.

Airflow directions and SC		[SC-A]		[SC-B]		[SC-C]		[SC-D]	
		0°	45°	90°	135°	180°	225°	270°	315°
North Façade	SD	0.21	-0.36	-0.63	-0.27	-0.17	-0.44	-0.50	-0.44
	PR	0.10	0.29	0.63	0.50	0.71	0.58	0.79	0.51
South Façade	SD	-0.34	-0.30	-0.60	-0.45	0.89	-0.18	-0.54	-0.46
	PR	0.40	0.40	0.63	0.10	0.21	0.54	0.76	0.37

Table 9
Contaminant analysis results.

Scenario Categories	Scenarios	PR	SD	Model-based workflow				Empirical and hybrid workflow			
				CCL_{total} (#/m^3)	CCL_{BR} (#/m^3)	t_{dis} (HH: MM)	t_{inf} (HH: MM)	CCL_{total} (#/m^3)	CCL_{BR} (#/m^3)	t_{dis} (HH: MM)	t_{inf} (HH: MM)
SC-1	**SC-1A**	-	-	139	123	11:35	9:45	85	84	11:00	9:55
	SC-1B			220	179	13:30	9:40	456	429	16:10	9:35
	SC-1C			76	86	11:15	10:00	29	48	10:15	-
	SC-1D			198	151	12:10	9:40	501	511	18:05	9:35
SC-2	**SC-2A**	60%	40	148	125	11:45	9:45	85	85	10:55	9:55
	SC-2B		cm	230	184	13:20	9:35	445	424	16:05	9:35
	SC-2C			49	62	11:15	-	31	49	10:15	-
	SC-2D			192	153	12:00	9:40	472	484	16:00	9:30
SC-3	**SC-3A**	40%	40	142	120	11:40	9:50	82	84	10:50	9:50
	SC-3B		cm	234	169	12:35	9:35	584	851	18:10	9:30
	SC-3C			99	93	11:35	10:00	30	48	10:15	-
	SC-3D			249	212	12:35	9:30	404	410	16:00	9:30
SC-4	**SC-4A**	60%	60	145	123	11:45	9:45	82	84	10:50	9:50
	SC-4B		cm	226	178	13:15	9:40	550	526	18:05	9:35
	SC-4C			50	64	11:15	-	33	52	10:15	-
	SC-4D			190	150	12:00	9:40	438	431	16:10	9:35
SC-5	**SC-5A**	40%	60	68	101	10:45	10:00	82	84	10:50	9:55
	SC-5B		cm	235	172	12:30	9:35	547	550	18:05	9:30
	SC-5C			209	195	12:20	9:30	29	47	10:50	-
	SC-5D			240	201	12:30	9:30	421	422	16:00	9:30
SC-6	**SC-6A**	60%	80	137	117	11:40	9:50	82	84	10:50	9:50
	SC-6B		cm	235	189	13:10	9:35	494	478	16:15	9:35
	SC-6C			172	144	12:15	9:45	34	53	10:15	-
	SC-6D			139	118	11:50	9:50	417	412	16:00	9:35
SC-7	**SC-7A**	40%	80	143	121	11:40	9:45	89	88	11:00	9:50
	SC-7B		cm	237	177	12:30	9:35	522	522	18:00	9:30
	SC-7C			210	195	12:20	9:30	30	49	10:15	-
	SC-7D			240	201	12:30	9:30	411	398	16:00	9:35

shading devices placed on only one façade, PR is more influential on the façade located on the opposite of the façade with shading devices. On the other hand, SD is particularly influential on the façade with shading devices.

PIV analysis: PIV tests are performed only for SC-A (airflow from 0°) and SC-C (airflow from 180°) since they can receive tracer particles due to the perpendicular airflow towards the openings. However, the airflows from 90° to 270°, acting directly upon the blind W and E façades do not allow tracer particles to penetrate inside the test section. PIV results are inspected for airflow behavior and indoor airflow velocity due to the impact of different shading devices. The building core is blanked since there is no observed airflow

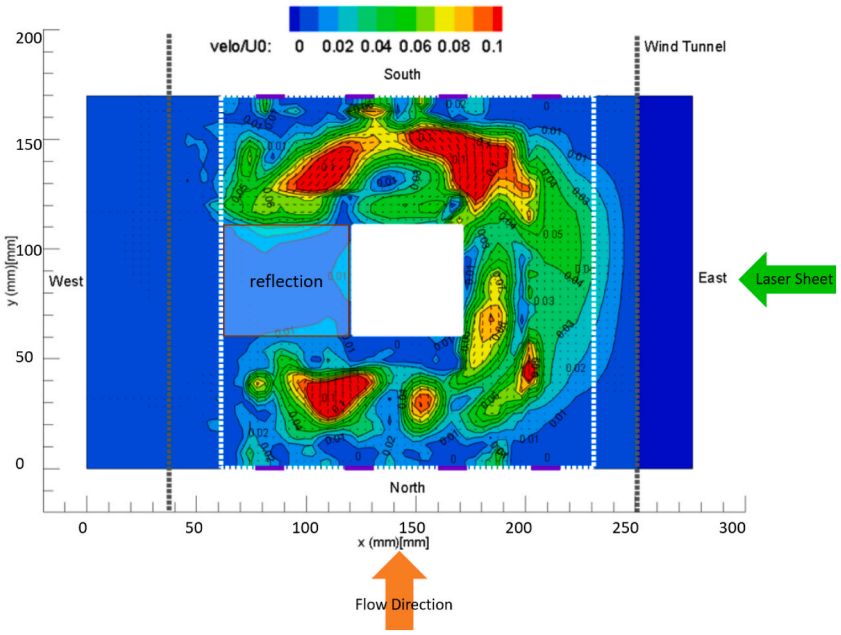

Fig. 20. PIV sample velocity field for SC-1A (Velo/U0 is the velocity magnitude normalized with the free-stream velocity).

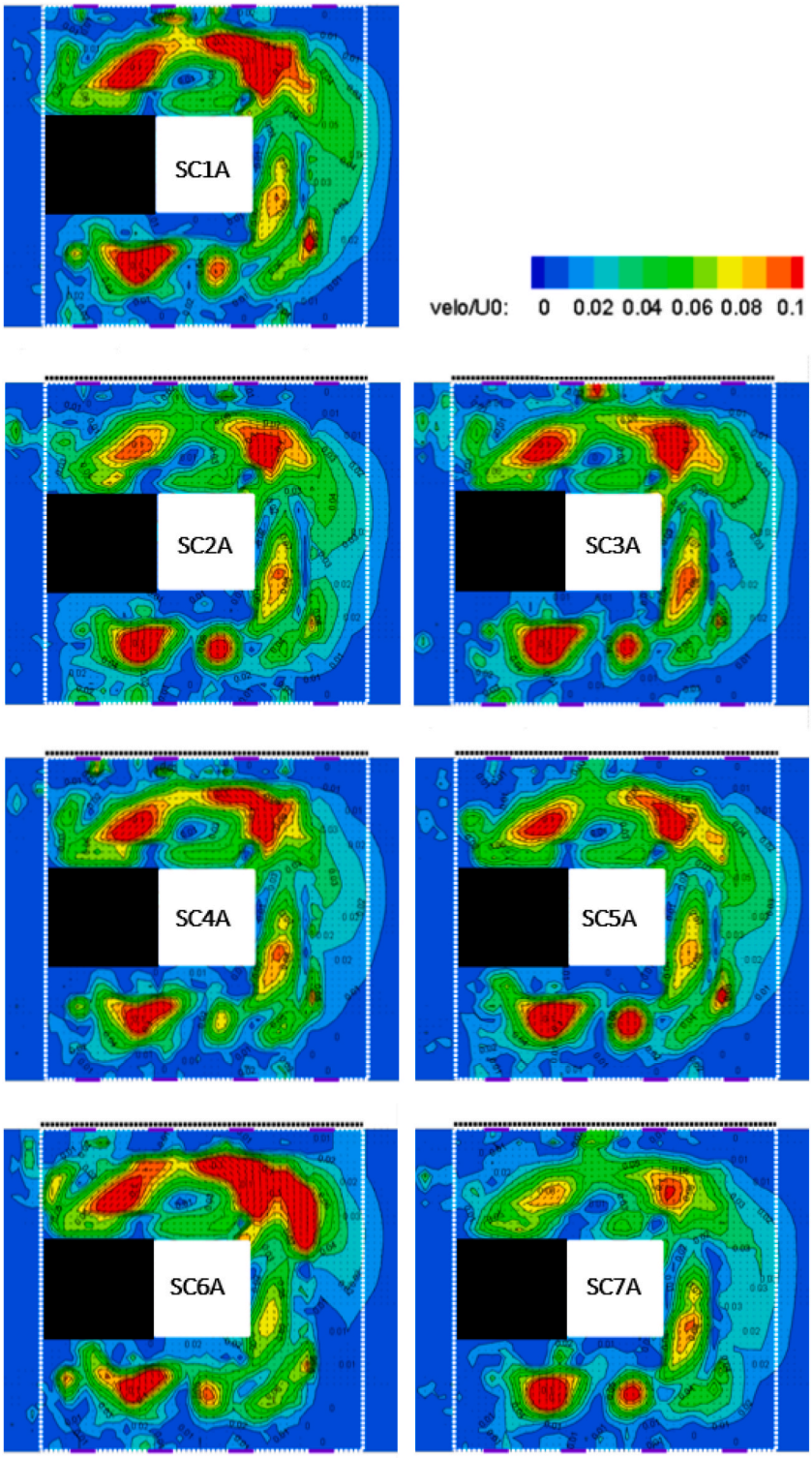

Fig. 21. Velocity field for North wind direction (SC-A).

leakage. The airflow behavior in the marked area could not be observed due to the excessive reflections and shadows in that region during the experiments (Fig. 20).

SC-A: Experiment results suggest that, except for SC6A, the shading devices reduce indoor airspeed (Fig. 21). There is a positive

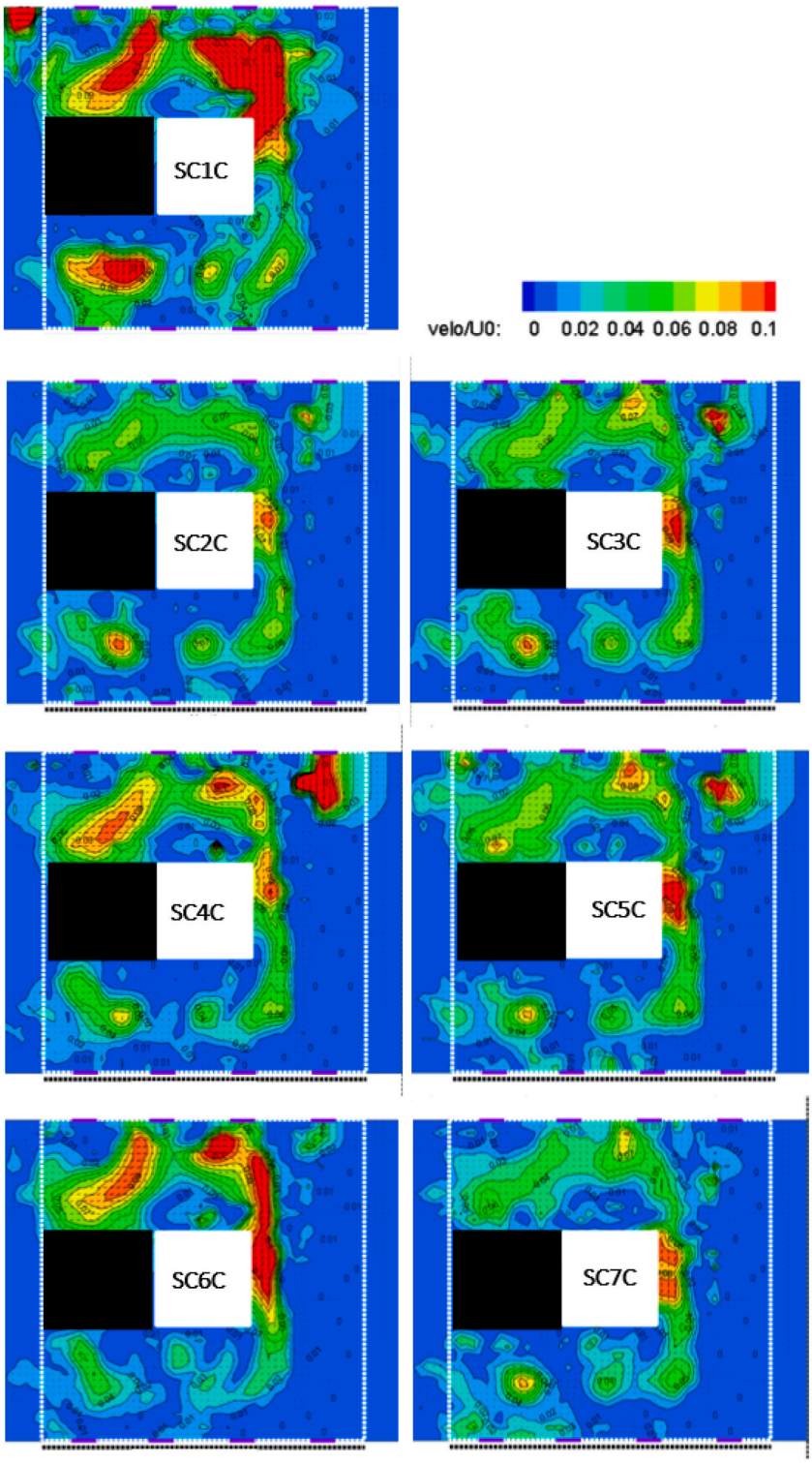

Fig. 22. Velocity field for South wind direction (SC-C).

correlation for SC-2A, SC-4A and SC-6A, whereas there is a negative correlation for SC-3A, SC-5A and SC-7A between the average indoor airspeed and the SD. Among the cases with the same SD but different PR, (i) there is a negative correlation between average indoor airspeed and PR in SC-2A and SC-3A, (ii) there is a positive correlation between average indoor airspeed and PR in SC-4A, SC-5A, SC-6A and SC-7A.

SC-C: Shading devices reduce indoor airspeed in all scenarios compared to the SC-1C (Fig. 22). There is a positive correlation between average indoor airspeed and the SD in SC-2C, SC-4C and SC-6C. Among the SC with the same SD but different PR, (i) there is a negative correlation between the average indoor airspeed and PR in SC-2C and SC-3C and (ii) there is a positive correlation between the average indoor airspeed and PR in SC-4A, SC-5A, SC-6A and SC-7A.

4.1.4. Contaminant analysis

The results are given for the implemented workflows while the comparative analysis is performed and correlations are calculated based on the hybrid workflow (Table 9). CCL_{total}, CCL_{BR}, t_{inf} and t_{dis} are calculated for all scenarios based on the contaminant analysis. t_{inf} is calculated based on CCL_{BR} since most of the respiratory activity occurs in this zone (h = 1.20–1.80 m). t_{dis} is calculated based on CCL_{total}. Three distinct contaminant accumulation behavior for CCL_{total} is identified among the scenarios: (1) steep peak until 10:00 as evident in SC-B and SC-D, (2) mild peak until 10:00 as evident in SC-A and (3) a horizontal stretch as evident in SC-C (Fig. 23). In all scenarios, CCL_{total} started to decrease with the contaminant's exit from the room at 10:00. The simulation results suggest that contaminant accumulation is 5% higher due to CCL in the BZ as compared to the entire room. SC-C results in the lowest CCL_{total} (2.7-fold, 16.5-fold and 14.1-fold lower as compared to SC-A, B and D, respectively). SC-C requires an average of 1H20M to complete contaminant discharge, which is 6H30M shorter t_{dis} than SC-B and SC-D on average and 0H30M shorter t_{dis} than SC-A on average. SC-C does not result in infection risk. The results of SC-A are similar to C-scenarios, resulting in the second lowest CCL_{total} value (64% higher than SC-C) and the second shortest t_{dis} (~1H55M). On the contrary, SC-B and SC-D result in the highest CCL_{total} values. The analysis suggests that direct airflow upon the façades with openings can considerably decrease indoor air contamination (Fig. 24). Indirect airflows increase the contaminant transport and circulate the contaminant inside the room for a longer time, posing relatively higher infection risks to occupants.

Airborne contamination is also evaluated for SD and PR. Analysis results suggest that there is a weak negative correlation (p = -25) between PR and CCL_{total} whereas there is a medium positive correlation (p = 0.31) between SD and CCL_{total}. Similarly, there is a medium negative correlation (p = -0.34) between PR and CCL_{BR} whereas there is a medium positive correlation (p = 0.42) between SD and CCL_{BR}. t_{dis} has a weak negative correlation (p = -0.22) and a weak positive correlation (p = 0.27) with PR and SD, respectively. No correlation has been found between t_{dis} and PR (p = 0.0) whereas there is a medium negative correlation (p = -0.43) between t_{dis} and SD.

4.2. Reducing the design search space with the hybrid workflow: overall comparison of shading configurations

In this study, we perform daylighting, energy, CFD simulations and WTT experiments for all scenarios. Nevertheless, in the pipeline, there are several assessment stages that remove the scenarios remaining below the performance thresholds. If applied to the case study, SC-3, SC-5 and SC-7 are the first three scenarios that can be eliminated as they score the lowest in DLA (39.8%, 37.4% and 37.2%, respectively). Accordingly, SC-2, SC-4 and SC-6 are selected for the CFD and energy simulations. The energy analysis results of SC-2, SC-4 and SC-6 show similar T_i, ventilation-sensible heat loss and ACH values. They remained within the comfort zone of natural

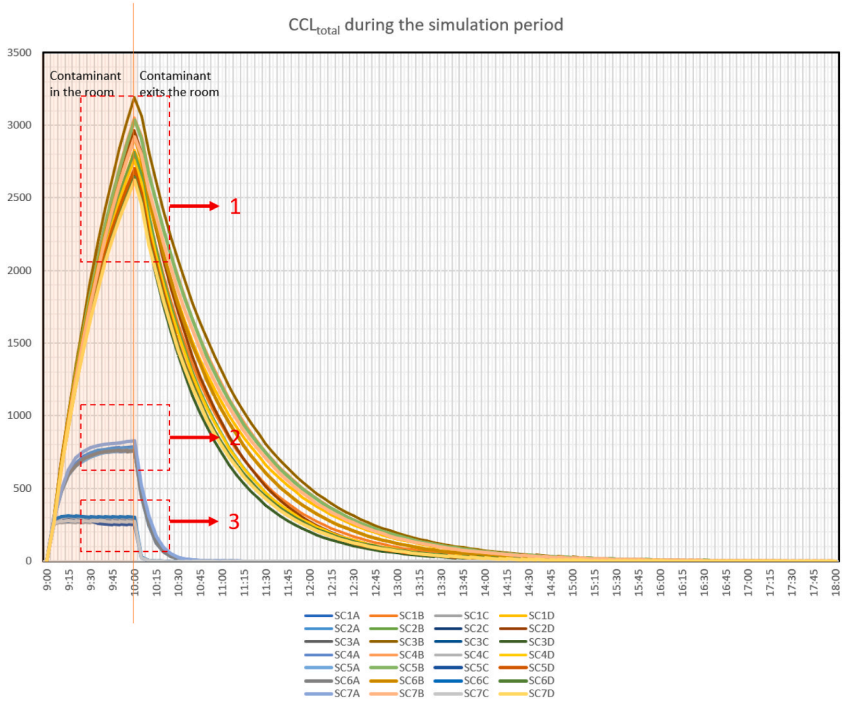

Fig. 23. CCL_{total} of scenarios during the simulation period (1) steep peak until 10:00, (2) mild peak until 10:00 and (3) a horizontal stretch.

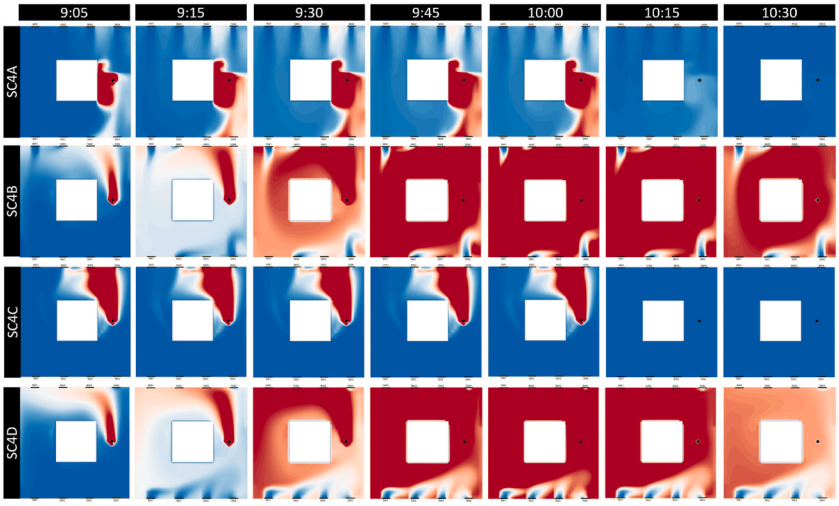

Fig. 24. Sample mapping of contaminant dispersion behavior (A, B, C and D scenarios of SC-4).

ventilation in Ankara. In this respect, wind tunnel tests are performed for SC-2, SC-4 and SC-6. WTT-corrected energy simulations result in similar values for SC-2, SC-4 and SC-6. However, while SC-2 and SC-6 showed similar CCL_{total}, CCL_{BR}, t_{dis} and t_{inf}, SC-4 resulted in higher values, posing higher infection risks to the occupants. Between SC-2 and SC-6, SC-2 can be selected as the final shading configuration due to its relatively better daylighting, ventilation-sensible heat loss and contaminant discharge performance. Amongst the SC-2 scenarios, SC-2C resulted in the lowest CCL_{total} and CCL_{BR}, requiring shorter t_{dis} as compared to SC-2A-B-D (Table 10). In this respect, SC-2C is found to be the best-performing scenario.

4.3. The impact of the error between CFD and wind tunnel on performance metrics

Error analysis is performed for the energy and contaminant simulations. C_p results obtained from CFD and WTT are used as inputs for the energy and contaminant analyses. The aim is to calculate the impact of the error between CFD and WTT results on energy performance and contaminant parameters. Mean absolute percent error (MAPE) is calculated for C_p, T_i, ACH, Q_{vent} and CCL_{total} to investigate how far apart the CFD-corrected simulation results are from the WTT-corrected simulation results in a regression analysis. MAPE is first calculated for the average values of the abovementioned parameters, then for each dataset of each scenario to investigate the error of the two distinct tools regarding the different (1) wind direction-shading, (2) SD and (3) PR.

MAPE is calculated as −58.90% for all C_p values obtained from CFD and WTT, which could also be referred to as the validation of CFD simulations. MAPE is also calculated for each scenario category to investigate the impact of the shading design variables on the error (Table 11). For SC-1, SC-2, SC-4 and SC-6, MAPE is calculated as in Table 11, which is 10.06% on average. On the other hand, MAPE is calculated for SC-3, SC-5 and SC-7 as 124.20% on average, which is 12.4 times higher than SC-1-2-4 and 6. As the MAPE results suggest, there is a strong negative correlation ($r = -0.73$) between the PR and error values. If PR is high, then the percent error value is calculated more accurately as compared to the scenarios with low PR values. No correlation is found between SD and percent error.

Table 10
Comparison of SC-2 and SC-6.

SC	PR	SD	DLA	UDI	DGP	T_i	CO_2	Q_{vent}	ACH	CCL $_{total}$	CCL $_{BR}$	t_{dis}	t_{inf}
SC-2	60%	40 cm	76.4	79.3	0.27	25.9	409	2695	19	258	260	13:18	0H30M
SC-6	60%	80 cm	48.7	81.9	0.27	25.9	410	2590	19	256	256	13:20	0H30M
SC-2 scenarios													
SC-2A						24.8	316	3508	31	85	85	10:55	0H55M
SC-2B						27.1	504	1897	5	445	424	16:06	0H35M
SC-2C						24.8	317	3466	31	31	49	10:15	0H00M
SC-2D						27.1	499	1908	6	472	484	16:00	0H30M

Table 11
MAPE of C_p values for each scenario category.

Scenario Categories	SC-1	SC-2	SC-3	SC-4	SC-5	SC-6	SC-7
MAPE of C_p values	-11.44%	-10.07%	-136.29%	-9.61%	-119.63%	-9.14%	-116.68%
PR	100% (no shading)	60%	40%	60%	40%	60%	40%

MAPE of T_i and Q_{vent} resulted in 3.15% and 1.55%, which demonstate a good agreement between the two datasets, while ACH and CCL_{total} showed a more significant error percentage of 15.43% and 86.25% respectively (Table 12). Based on the analysis results, it is observed that CFD simulations underestimate CCL_{total}, ACH and Q_{vent} while correspondingly overestimating T_i values. MAPE is also calculated for each scenario category (Table 13) and each simulated scenario (Fig. 25). ACH and CCL_{total} resulted in a higher error percentage than the T_i and Q_{vent}. The scenarios which receive wind on the façade with the shading (SC-C) resulted in the highest error percentage for T_i, ACH and Q_{vent} whereas the lowest error percentage for CCL_{total}. The results indicate that the accuracy of airflow-related data must be augmented with WTT, particularly for the building façades where the wind interacts with auxiliary building elements such as shading devices. In this respect, the hybrid pipeline can be implemented to rectify/increase the accuracy of the airflow-related data. The results also suggest that there is a weak negative correlation between PR and T_i ($r = -0.35$), ACH ($r = -0.38$), Q_{vent} ($r = -0.32$), and a weak positive correlation between PR and CCL_{total} ($r = 0.26$) respectively. The scenarios with 60% PR resulted

Table 12
MAPE calculated for overall results of T_i, Q_{vent}, ACH and CCL_{total}.

Metrics	MAPE	Average analysis results for CFD-corrected	Average analysis results for WTT-corrected
T_i	3.15%	27 °C	26 °C
Q_{vent}	1.55%	2799 W	2834 W
ACH	15.43%	17 ACH	19 ACH
CCL_{total}	86.25%	173 #/m^3	267 #/m^3

Table 13
MAPE calculated for each scenario category of T_i, Q_{vent}, ACH, and CCL_{total}.

Scenario Categories	T_i	ACH	Q_{vent}	CCL_{total}
SC-A	0.06%	3.78%	0.50%	37.90%
SC-B	0.11%	4.15%	1.95%	122.40%
SC-C	0.42%	14.45%	4.06%	64.90%
SC-D	0.07%	2.66%	0.90%	119.75%

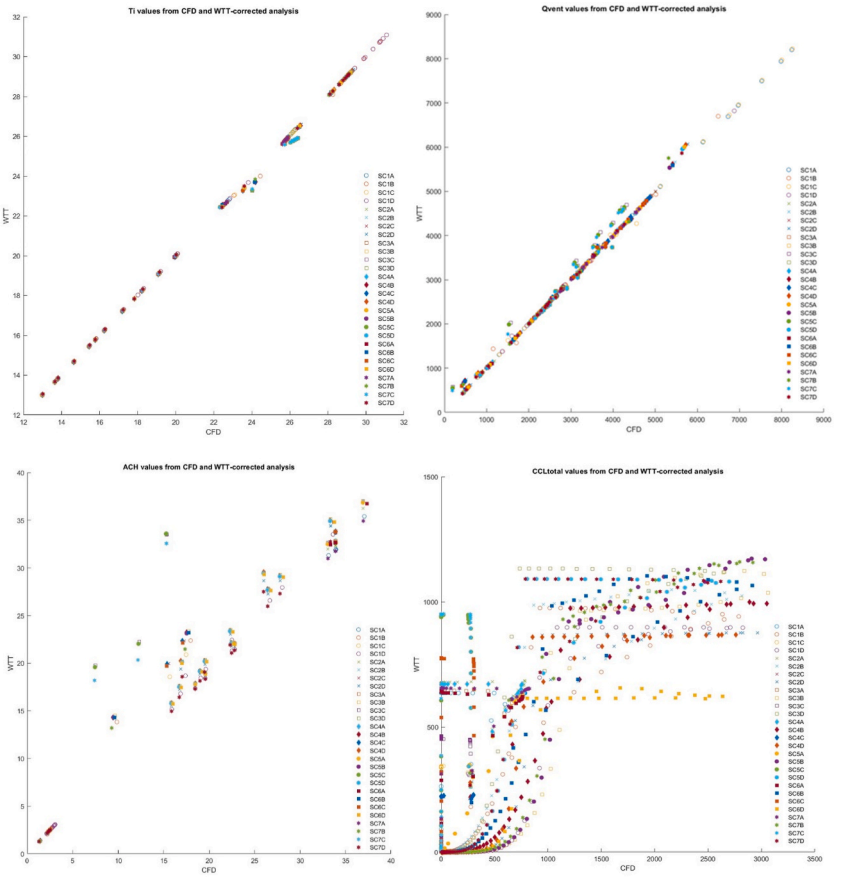

Fig. 25. Error graphics for T_i *(upper-left)*, Q_{vent} *(upper-right)*, ACH *(lower-left)* and CCL_{total} *(lower-right)*.

in 70.4%, 65.1%, 51.1% and 68.38% lower errors than the scenarios with 40% PR, for T_i, *ACH,* Q_{vent} and CCL_{total} respectively. On the other hand, similar to the C_p, no correlation has been found between the error percentage and SD. MAPE results demonstrate that empirical and hybrid workflows can lead to accurate analysis results and perform well with airflow-related data.

4.4. Findings

The hybrid workflow has shown to improve the accuracy of energy and contaminant analysis results by providing accurate microclimatic data based on T_i and C_p values. The error analysis in section 4.3 shows integrating wind tunnel measurements is required to correct the CFD results to improve the accuracy of C_p values. The error analysis also showed that airflow-related performance measures resulted in a high error percentage despite the low error percentage between the CFD-corrected and WTT-corrected energy analyses. In this respect, this research shows that wind tunnel measurements increase the accuracy of airflow-related data. Also, this research agrees with the literature on using wind tunnel measurements for accurate C_p and performance analysis results. As a result, CFD tools integrated into 3D design environments can be used for preliminary performance feedback while wind tunnel measurements can be used during the later stages of the performance evaluation in order to increase the accuracy of the results.

This paper also reports a number of findings concerning the impact of the shading configuration on performance metrics (Table 14):

Ventilation and contamination-related metrics: SD is observed to reduce ACH, resulting in increased indoor contamination levels (CCL_{total} and CCL_{BR}). Contrarily, PR is observed to increase ACH, as a result of which indoor contamination (CCL_{total} and CCL_{BR}) and the required time for the contaminant discharge (t_{dis}) are reduced. As expected, PR has a positive impact on delaying infection time. Regardless of the wind direction, shading devices reduce indoor airspeed (as compared to the baseline case). However, SD and PR characteristics are observed to influence indoor airspeed. SD increases indoor airspeed in the higher PR case (60%) whereas SD decreases indoor airspeed in the lower PR case (40%).

Energy-related metrics: SD is observed to reduce T_i and Q_{vent}. Contrarily, PR is observed to increase T_i and Q_{vent}. The deeper shading devices can reduce indoor air temperature by reducing solar exposure, but at the same time, they can reduce ventilation-sensible heat loss by reducing the air change rate. The shading devices with a higher perforation ratio increase indoor air temperature due to the relatively higher solar exposure. Also, shading devices with higher PR increase ventilation-sensible heat loss by increasing the air change rate. Therefore, it is crucial to consider both the shading depth and perforation ratio regarding the impact of solar exposure and ventilation-sensible heat loss on indoor air temperature.

Daylighting-related metrics: SD has a negative impact on DLA and UDI whereas SD is observed to reduce glare. Contrarily, PR has a positive impact on daylight illuminations. However, higher PR runs the risk of glare problems for the occupants.

5. Conclusion

This research presented a computational pipeline for performance-based design, which is an integrated building performance analysis framework, that can be utilized in three different workflows regarding the airflow calculation method: model-based, empirical-based, and hybrid. The pipeline couples 3D parametric design, daylighting, CFD, energy and contaminant analysis with wind tunnel tests. The contribution and the novelty of the pipeline is four-fold as follows:

Multi-criteria assessment: The developed pipeline enables multi-criteria performance assessment of ventilation, energy and daylighting performance metrics. The pipeline manages the data flow between the tools, aiming to support complex performance-based design processes involving different tools.

Integration of computational and physical testing methods: The pipeline increases the accuracy of airflow-related data by coupling computational and physical testing methods, where both methods have their own advantages and disadvantages. With the developed pipeline both methods are combined to overcome the drawbacks of using either method alone.

Calculating the impact of auxilary façade elements on building energy performance metrics: The developed pipeline for a hypothetical open office with shading devices and their impact on building performance, focusing on energy, NV, air contamination and daylighting measures are evaluated. Modeling the shading devices is considerably significant for accurate performance feedback, which improved the accuracy of airflow-related data and, therefore, relatively more reliable performance analysis results were obtained. If the shading devices had not been not modeled for CFD simulations, the results would have overestimated the ventilation rate (ACH) by around 85%. Similarly, if the shading devices had not been tested in WTT, the results would have underestimated the ventilation rate by around 1.4%.

Managing design search space and simulation workload: This research presents a number of practical implications of the developed pipeline. First, utilizing 3D parametric tools and integrated analysis tools facilitated managing design alternatives and the simulation workload. Also, the pipeline is implemented in stages due to complexity and computational costs. Implementing in stages facilitated managing the simulation workload by reducing the size of the design search space. During a design process, exploring a very high number of design alternatives is not practical due to the computational cost of analysis. The proposed method can be used to first reduce design search space to a limited number of design alternatives, followed by the WTT for a few promising alternatives. We

Table 14
Relationship between performance parameters and shading parameters.

	Daylighting			Energy		Ventilation				
	DGP	DLA	UDI	T_i	Q_{vent}	ACH	CCL_{total}	CCL_{BR}	t_{dis}	t_{inf}
SD	-0.57	-0.42	-0.43	-0.44	-0.45	-0.46	-0.36	-0.57	0.02	0.27
PR	0.77	0.83	0.72	0.85	0.88	0.42	-0.37	-0.52	-0.72	0.89

anticipate that such high accuracy levels and the physical/computational cost of analysis can be undertaken for mission-critical or super-tall buildings. For relatively low-risk projects with limited time and budget, the accuracy of CFD testing may suffice and the pipeline can be implemented without WTT. Our pipeline can also be used for elements other than shading devices that are expected to influence the airflow, therefore, natural ventilation performance.

This research also has several limitations. Despite the pipeline indicates design integration, the trade-offs between the performance parameters remain limited to explore. The pipeline can be revised and extended by integrating metrics and tools which can be further explored. Future research work can explore the effective use of data-driven methods such as machine learning for effective design space exploration in relation to integrated performance assessment.

Funding

This research did not receive any specific grant from funding agencies in the public, commercial, or not-for-profit sectors.

CRediT authorship contribution statement

Günsu Merin Abbas: Conceptualization, Methodology, Writing – original draft, Investigation, Methodology, Software, Visualization, Data curation. **Ipek Gursel Dino:** Supervision, Conceptualization, Methodology, Writing – review & editing. **Mustafa Percin:** Supervision, Conceptualization, Methodology, Writing – review & editing, Resources.

Declaration of competing interest

The authors declare that they have no known competing financial interests or personal relationships that could have appeared to influence the work reported in this paper.

Data availability

No data was used for the research described in the article.

Acknowledgements

The authors would like to thank METU RÜZGEM for making wind tunnel facilities available for this research. The authors would like to thank Dr. Oğuz Uzol, Dr. Nilay Uzol and the METU RÜZGEM team for their support throughout this research.

Appendix A. Supplementary data

Supplementary data to this article can be found online at https://doi.org/10.1016/j.jobe.2023.106991.

References

[1] F. Allard, Natural Ventilation in Buildings: A Design Handbook, James&James, London, 1998.
[2] EPA, Reference Guide for Indoor Air Quality in Schools, 2021. https://www.epa.gov/iaq-schools/reference-guide-indoor-air-quality-schools.
[3] ASHRAE, Indoor Air Quality Guide: Best Practices for Design, Construction, and Commissioning, American Society of Heating, Refrigerating and Air-Conditioning Engineers, Inc., Atlanta, 2009.
[4] V. Hartkopf, A. Aziz, V. Loftness, Facades and enclosures, building for sustainability, in: V. Loftness, D. Haase (Eds.), Sustainable Built Environments, Springer, New York, 2012, pp. 163–193.
[5] J.K. Calautit, B.R. Hughes, Wind tunnel and CFD study of the natural ventilation performance ofa commercial multi-directional wind tower, Build. Environ. 80 (2014) 71–83, https://doi.org/10.1016/j.buildenv.2014.05.022.
[6] A. Aflaki, M. Esfandiari, S. Mohammadi, A review of numerical simulation as a precedence method for prediction and evaluation of building ventilation performance, Sustainability (2021) 13, https://doi.org/10.3390/su132212721.
[7] A. Malkawi, G. Augenbroe, Advanced building simulation, Simulation 1 (2003) 119–121, https://doi.org/10.4324/9780203684009.
[8] I.G. Dino, R. Stouffs, Evaluation of reference modeling for building performance assessment, Autom. ConStruct. 40 (2014) 44–59, https://doi.org/10.1016/j.autcon.2013.12.007.
[9] P. de Wilde, Building Performance Analysis, John Wiley & Sons, New Jersey, 2018.
[10] J.A. Clarke, J.L.M. Hensen, Integrated building performance simulation: progress, prospects and requirements, Build. Environ. 91 (2015) 294–306, https://doi.org/10.1016/j.buildenv.2015.04.002.
[11] J.A. Clarke, J.L.M. Hensen, Integrated building performance simulation: progress, prospects and requirements, Build. Environ. 91 (2015) 294–306, https://doi.org/10.1016/j.buildenv.2015.04.002.
[12] B.J. Futrell, E.C. Ozelkan, D. Brentrup, Optimizing complex building design for annual daylighting performance and evaluation of optimization algorithms, Energy Build. 92 (2015) 234–245, https://doi.org/10.1016/j.enbuild.2015.01.017.
[13] D.A. Chi, D. Moreno, J. Navarro, Design optimisation of perforated solar façades in order to balance daylighting with thermal performance, Build. Environ. 125 (2017) 383–400, https://doi.org/10.1016/j.buildenv.2017.09.007.
[14] S. Motamedi, P. Liedl, Integrative algorithm to optimize skylights considering fully impacts of daylight on energy, Energy Build. 138 (2017) 655–665, https://doi.org/10.1016/j.enbuild.2016.12.045.
[15] İ. Gürsel Dino, G. Üçoluk, Multiobjective design optimization of building space layout, energy, and daylighting performance, J. Comput. Civ. Eng. (2017) 31.
[16] M. Ferrara, E. Sirombo, E. Fabrizio, Energy & Buildings Automated optimization for the integrated design process : the energy , thermal and visual comfort nexus, Energy Build. 168 (2018) 413–427, https://doi.org/10.1016/j.enbuild.2018.03.039.
[17] E. Touloupaki, T. Theodosiou, Performance simulation integrated in parametric 3D modeling as a method for early stage design optimization- A review, Energies 10 (2017), https://doi.org/10.3390/en10050637.

[18] N. Delgarm, B. Sajadi, S. Delgarm, Multi-objective optimization of building energy performance and indoor thermal comfort : a new method using artificial bee colony (ABC), Energy Build. 131 (2016) 42–53, https://doi.org/10.1016/j.enbuild.2016.09.003.

[19] T. Østergård, R.L. Jensen, S.E. Maagaard, Early Building Design : informed decision-making by exploring multidimensional design space using sensitivity analysis, Energy Build. 142 (2017) 8–22, https://doi.org/10.1016/j.enbuild.2017.02.059.

[20] H.M. Taleb, Natural ventilation as energy efficient solution for achieving low-energy houses in Dubai, Energy Build. 99 (2015) 284–291, https://doi.org/10.1016/j.enbuild.2015.04.019.

[21] J. Song, X. Huang, D. Shi, W.E. Lin, S. Fan, P.F. Linden, Natural ventilation in London: towards energy-efficient and healthy buildings, Build. Environ. 195 (2021), 107722, https://doi.org/10.1016/j.buildenv.2021.107722.

[22] E. Sanchez, A. Rolando, R. Sant, L. Ayuso, Influence of Natural Ventilation Due to Buoyancy and Heat Transfer in the Energy Efficiency of a Double Skin Facade Building, 33, Energy for Sustainable Development, 2016, pp. 139–148, https://doi.org/10.1016/j.esd.2016.02.002.

[23] A.U. Weerasuriya, X. Zhang, V.J.L. Gan, Y. Tan, A holistic framework to utilize natural ventilation to optimize energy performance of residential high-rise buildings, Build. Environ. 153 (2019) 218–232, https://doi.org/10.1016/j.buildenv.2019.02.027.

[24] J.K. Calautit, D. O'Connor, P.W. Tien, S. Wei, C.A.J. Pantua, B. Hughes, Development of a natural ventilation windcatcher with passive heat recovery wheel for mild-cold climates: CFD and experimental analysis, Renew. Energy 160 (2020) 465–482, https://doi.org/10.1016/j.renene.2020.05.177.

[25] R.M.S.F. Almeida, M. Pinto, P.G. Pinho, L.T. de Lemos, Natural ventilation and indoor air quality in educational buildings: experimental assessment and improvement strategies, Energy Effic 10 (2017) 839–854, https://doi.org/10.1007/s12053-016-9485-0.

[26] A.M. Papadopoulos, A. Avgelis, Indoor environmental quality in naturally ventilated office buildings and its impact on their energy performance, Int. J. Vent. 2 (2003) 203–212, https://doi.org/10.1080/14733315.2003.11683665.

[27] C. Heracleous, A. Michael, Experimental assessment of the impact of natural ventilation on indoor air quality and thermal comfort conditions of educational buildings in the Eastern Mediterranean region during the heating period, J. Build. Eng. 26 (2019), 100917, https://doi.org/10.1016/j.jobe.2019.100917.

[28] P. Spiru, P.L. Simona, A review on interactions between energy performance of the buildings, outdoor air pollution and the indoor air quality, Energy Proc. 128 (2017) 179–186, https://doi.org/10.1016/j.egypro.2017.09.039.

[29] Z. Luo, J. Zhao, J. Gao, L. He, Estimating natural-ventilation potential considering both thermal comfort and IAQ issues, Build. Environ. 42 (2007) 2289–2298, https://doi.org/10.1016/j.buildenv.2006.04.024.

[30] B. Hamzah, M.T. Ishak, S. Beddu, M.Y. Osman, Thermal comfort analyses of naturally ventilated university classrooms, Struct. Surv. 34 (2016) 427–445, https://doi.org/10.1108/SS-12-2015-0055.

[31] S. Omrani, V. Garcia-Hansen, B.R. Capra, R. Drogemuller, Effect of natural ventilation mode on thermal comfort and ventilation performance: full-scale measurement, Energy Build. 156 (2017) 1–16, https://doi.org/10.1016/j.enbuild.2017.09.061.

[32] J.A. Castillo, G. Huelsz, A methodology to evaluate the indoor natural ventilation in hot climates: heat Balance Index, Build. Environ. 114 (2017) 366–373, https://doi.org/10.1016/j.buildenv.2016.12.027.

[33] R. Aynsley, Estimating summer wind driven natural ventilation potential for indoor thermal comfort, J. Wind Eng. Ind. Aerod. 83 (1999) 515–525, https://doi.org/10.1016/S0167-6105(99)00098-7.

[34] G.M. Abbas, I. Gursel Dino, The Impact of Natural Ventilation on Airborne Biocontaminants: a Study on COVID-19 Dispersion in an Open Office, Engineering, Construction and Architectural Management, 2021, https://doi.org/10.1108/ecam-12-2020-1047 ahead-of-p.

[35] C. for D.C. and P. CDC, Hierarchy of Controls, 2015. https://www.cdc.gov/niosh/topics/hierarchy/default.html. (Accessed 7 February 2021).

[36] L. Morawska, J.W. Tang, W. Bahnfleth, P.M. Bluyssen, A. Boerstra, G. Buonanno, J. Cao, S. Dancer, A. Floto, F. Franchimon, C. Haworth, J. Hogeling, C. Isaxon, J.L. Jimenez, J. Kurnitski, Y. Li, M. Loomans, G. Marks, L.C. Marr, L. Mazzarella, A.K. Melikov, S. Miller, D.K. Milton, W. Nazaroff, P.V. Nielsen, C. Noakes, J. Peccia, X. Querol, C. Sekhar, O. Seppänen, S. ichi Tanabe, R. Tellier, K.W. Tham, P. Wargocki, A. Wierzbicka, M. Yao, How can airborne transmission of COVID-19 indoors be minimised? Environ. Int. 142 (2020) https://doi.org/10.1016/j.envint.2020.105832.

[37] H. Nishiura, N.M. Linton, A.R. Akhmetzhanov, Serial interval of novel coronavirus (COVID-19) infections, Int. J. Infect. Dis. 93 (2020) 284–286, https://doi.org/10.1016/j.ijid.2020.02.060.

[38] T. Yang, D.J. Clements-Croome, Natural ventilationnatural ventilationin built environmentnatural ventilationin-built environment, in: R.A. Meyers (Ed.), Encyclopedia of Sustainability Science and Technology, Springer New York, New York, NY, 2012, pp. 6865–6896, https://doi.org/10.1007/978-1-4419-0851-3_488.

[39] T. Carleton, K. Meng, Causal Empirical Estimates Suggest COVID-19 Transmission Rates Are Highly Seasonal, 2020, https://doi.org/10.1101/2020.03.26.20044420. MedRxiv.

[40] N. Islam, S. Shabnam, A.M. Erzurumluoglu, Temperature, Humidity, and Wind Speed Are Associated with Lower Covid-19 Incidence, MedRxiv, 2020, pp. 8–11.

[41] D.K.A. Rosario, Y.S. Mutz, P.C. Bernardes, C.A. Conte-junior, Relationship between COVID-19 and weather: case study in a tropical country, Int. J. Hyg Environ. Health 229 (2020).

[42] A. Sanchez-Lorenzo, J. Vaquero-Martínez, J. Calbó, M. Wild, A. Santurtún, J.A. Lopez-Bustins, J.M. Vaquero, D. Folini, M. Antón, Anomalous Atmospheric Circulation Favored the Spread of Covid-19 in Europe, 2020, https://doi.org/10.1101/2020.04.25.20079590. ArXiv. 2020.

[43] A. Afshari, G. Hultmark, P. V Nielsen, A. Maccarini, Ventilation system design and the coronavirus (COVID-19), Front Built Environ 7 (2021), https://doi.org/10.3389/fbuil.2021.662489.

[44] L. Borro, L. Mazzei, M. Raponi, P. Piscitelli, A. Miani, A. Secinaro, The role of air conditioning in the diffusion of Sars-CoV-2 in indoor environments: a first computational fluid dynamic model, based on investigations performed at the Vatican State Children's hospital, Environ. Res. 193 (2020), 110343, https://doi.org/10.1016/j.envres.2020.110343.

[45] M. Guo, P. Xu, T. Xiao, R. He, M. Dai, S.L. Miller, Review and comparison of HVAC operation guidelines in different countries during the COVID-19 pandemic, Build. Environ. 187 (2021), 107368, https://doi.org/10.1016/j.buildenv.2020.107368.

[46] T. Lipinski, D. Ahmad, N. Serey, H. Jouhara, Review of ventilation strategies to reduce the risk of disease transmission in high occupancy buildings, International Journal of Thermofluids 7 (2020), 100045, https://doi.org/10.1016/j.ijft.2020.100045. –8.

[47] L.F. Pease, N. Wang, T.I. Salsbury, R.M. Underhill, J.E. Flaherty, A. Vlachokostas, G. Kulkarni, D.P. James, Investigation of potential aerosol transmission and infectivity of SARS-CoV-2 through central ventilation systems, Build. Environ. (2021), 107633, https://doi.org/10.1016/j.buildenv.2021.107633.

[48] J. Ren, Y. Wang, Q. Liu, Y. Liu, Numerical study of three ventilation strategies in a prefabricated COVID-19 inpatient ward, Build. Environ. 188 (2021), 107467, https://doi.org/10.1016/j.buildenv.2020.107467.

[49] P.K. Kundu, I.M. Cohen, H.H. Hu, Fluid Mechanics, third ed., Elsevier Academic Press, 2004.

[50] S. Charisi, T.K. Thiis, T. Aurlien, Full-scale measurements of wind-pressure coefficients in twin medium-rise buildings, Buildings 9 (2019), https://doi.org/10.3390/buildings9030063.

[51] D. Cóstola, B. Blocken, J.L.M. Hensen, Overview of Pressure Coefficient Data in Building Energy Simulation and Airflow Network Programs, 2009, p. 31.

[52] H. Dai, B. Zhao, Association of Infected Probability of COVID-19 with Ventilation Rates in Confined Spaces: A Wells-Riley Equation Based Investigation, 2020, https://doi.org/10.1101/2020.04.21.20072397. MedRxiv.

[53] A. Foster, M. Kinzel, Estimating COVID-19 exposure in a classroom setting: a comparison between mathematical and numerical models, Phys. Fluids 33 (2021), https://doi.org/10.1063/5.0040755.

[54] C. Sun, Z. Zhai, The efficacy of social distance and ventilation effectiveness in preventing COVID-19 transmission, Sustain. Cities Soc. 62 (2020), 102390, https://doi.org/10.1016/j.scs.2020.102390.

[55] G. Buonanno, L. Stabile, L. Morawska, Estimation of airborne viral emission: quanta emission rate of SARS-CoV-2 for infection risk assessment, Environ. Int. 141 (2020), 105794, https://doi.org/10.1016/j.envint.2020.105794.

[56] S. Maltezos, A. Georgakopoulou, Novel Approach for Monte Carlo Simulation of the New COVID-19 Spread Dynamics, 2020, pp. 1–9, https://doi.org/10.1101/2020.12.03.20243220. MedRxiv.

[57] M. Riediker, C. Monn, Simulation of sars-cov-2 aerosol emissions in the infected population and resulting airborne exposures in different indoor scenarios, Aerosol Air Qual. Res. 21 (2021) 1–14, https://doi.org/10.4209/aaqr.2020.08.0531.
[58] S. Triambak, D.P. Mahapatra, A random walk Monte Carlo simulation study of COVID-19-like infection spread, Physics 574 (2020), 126014, https://doi.org/10.1016/j.physa.2021.126014.
[59] G. Xie, A novel Monte Carlo simulation procedure for modelling COVID-19 spread over time, Sci. Rep. 10 (2020) 1–9, https://doi.org/10.1038/s41598-020-70091-1.
[60] W. Van Damme, R. Dahake, R. Van De Pas, G. Vanham, Y. Assefa, COVID-19: does the infectious inoculum dose-response relationship contribute to understanding heterogeneity in disease severity and transmission dynamics? Med. Hypotheses 146 (2021).
[61] T. Watanabe, T.A. Bartrand, M.H. Weir, T. Omura, C.N. Haas, Development of a dose-response model for SARS coronavirus, Risk Anal. 30 (2010) 1129–1138, https://doi.org/10.1111/j.1539-6924.2010.01427.x.
[62] X. Zhang, J. Wang, Dose-response Relation Deduced for Coronaviruses from COVID-19, SARS and MERS Meta-Analysis Results and its Application for Infection Risk Assessment of Aerosol Transmission, Clinical Infectious Diseases, 2020, pp. 1–5, https://doi.org/10.1093/cid/ciaa1675.
[63] G.N. Sze To, C.Y.H. Chao, Review and comparison between the Wells-Riley and dose-response approaches to risk assessment of infectious respiratory diseases, Indoor Air 20 (2010) 2–16, https://doi.org/10.1111/j.1600-0668.2009.00621.x.
[64] D. Etheridge, B. Ford, Natural ventilation of tall buildings: options and limitations, in: CTBUH 8th World Congress, 2008. Dubai.
[65] A. Kirimtat, B. Kundakci, I. Chatzikonstantinou, S. Sariyildiz, Review of simulation modeling for shading devices in buildings, Renew. Sustain. Energy Rev. 53 (2016) 23–49, https://doi.org/10.1016/j.rser.2015.08.020.
[66] A.A. Argiriou, C.A. Balaras, S.P. Lykoudis, Single-sided ventilation of buildings through shaded large openings, Energy 27 (2002) 93–115.
[67] K. Kosutova, T. Van van Hooff, C. Vanderwel, B. Blocken, J. Hensen, Cross-ventilation in a generic isolated building equipped with louvers : wind-tunnel experiments and CFD simulations, Build. Environ. 154 (2019) 263–280, https://doi.org/10.1016/j.buildenv.2019.03.019.
[68] J. Zheng, Q. Tao, L. Li, Numerical study of wind environment of a low-rise building with shading louvers: sensitive analysis and evaluation of cross ventilation, J. Asian Architect. Build Eng. 19 (2020) 541–558, https://doi.org/10.1080/13467581.2020.1758113.
[69] J. Lee, M. Alshayeb, J.D. Chang, A Study of Shading Device Configuration on the Natural Ventilation Efficiency and Energy Performance of a Double Skin Façade, 118, 2015, pp. 310–317, https://doi.org/10.1016/j.proeng.2015.08.432.
[70] N. Türkmenoğlu Bayraktar, V. Ok, Numerical evaluation of the effects of different types of shading devices on interior occupant thermal comfort using wind tunnel experimental data, Build. Simulat. 12 (2019) 683–696.
[71] M.S. Roudsari, C. Mackey, Ladybug Tools, 2012.
[72] R. Ramponi, B. Blocken, CFD simulation of cross-ventilation for a generic isolated building : impact of computational parameters, Build. Environ. 53 (2012) 34–48, https://doi.org/10.1016/j.buildenv.2012.01.004.
[73] CIBSE, Ventilation and Ductwork CIBSE Guide B2, 2016, 2016.
[74] U.S. Department of Energy's (DOE), Building Technologies Office (BTO), EnergyPlus, 2001.
[75] CIBSE, Environmental Design CIBSE Guide A, CIBSE Publications, 2006.
[76] W.S. Dols, B.J. Polidoro, CONTAM User Guide and Program Documentation - Version 3.2 (NIST Technical Note 1887), 2015, p. 330.
[77] P. Ruffles, Lighting Guide: Office Lighting, The Society of Light and Lighting, CIBSE, 2005.
[78] Radiance, Radiance, Radsite. https://www.radiance-online.org/about, 2019.
[79] J. Mardaljevic, L. Heschong, E.S. Lee, Daylight Metrics and Energy Savings, Lighting Research and Technology, 2009, pp. 1–23.
[80] En17037, European Standard EN17037: Daylight in Buildings, 2018.
[81] Robert McNeel, Rhinoceros Associates. https://www.rhino3d.com/6/features#beyond, 2020.
[82] D. Rutten, Grasshopper 3D, 2007.
[83] The OpenFOAM Foundation, OpenFOAM User Guide, 2018, p. v1812.
[84] Ladybug Tools LLC, Ladybug tools-butterfly (n.d.), https://www.ladybug.tools/butterfly.html.
[85] A. de Myttenaere, B. Golden, B. Le Grand, F. Rossi, Mean absolute percentage error for regression models, Neurocomputing 192 (2016) 38–48, https://doi.org/10.1016/j.neucom.2015.12.114.
[86] J. Franke, A. Hellsten, K.H. Schlünzen, B. Carissimo, The COST 732 Best Practice Guideline for CFD simulation of flows in the urban environment: a summary, Int. J. Environ. Pollut. 44 (2011) 419–427, https://doi.org/10.1504/IJEP.2011.038443.
[87] The OpenFOAM Foundation, OpenFOAM User Guide, 2018, p. v1812.
[88] C. Mackey, M.S. Roudsari, The tool (s) versus the toolkit, Humanizing Digital Reality 2 (2018).
[89] M. Marschall, J. Burry, F. Tahmasebi, Simulating natural ventilation in early stage design: combining an occupant behavior model with an airflow network approach, in: C. Gengnagel, O. Baverel, J. Burry, M. Ramsgaard Thomsen, S. Weinzierl (Eds.), Impact: Design with All Senses, Springer International Publishing, Cham, 2020, pp. 119–131.
[90] U.S. Department, Of Energy, EnergyPlus Documentation Engineering Reference, 2015, pp. 1996–2015.
[91] D. Cóstola, B. Blocken, J.L.M. Hensen, Overview of Pressure Coefficient Data in Building Energy Simulation and Airflow Network Programs, 2009, p. 31.
[92] NIST, CONTAM Weather File Creator. https://pages.nist.gov/CONTAM-apps/software/WEATHERprogram.htm, 2010.
[93] W.S. Dols, B.J. Polidoro, D. Poppendieck, S.J. Emmerich, NIST Technical Note 2095 A Tool to Model the Fate and Transport of Indoor Microbiological Aerosols, FaTIMA), 2020, https://doi.org/10.6028/NIST.TN.2095.
[94] N.H.L. Leung, D.K.W. Chu, E.Y.C. Shiu, K.H. Chan, J.J. McDevitt, B.J.P. Hau, H.L. Yen, Y. Li, D.K.M. Ip, J.S.M. Peiris, W.H. Seto, G.M. Leung, D.K. Milton, B. J. Cowling, Respiratory virus shedding in exhaled breath and efficacy of face masks, Nat. Med. 26 (2020) 676–680, https://doi.org/10.1038/s41591-020-0843-2.
[95] W.S. Dols, B.J. Polidoro, CONTAM 3.0 Tutorial, 2010.
[96] L.L. Wang, W.S. Dols, Q. Chen, AN introduction to the CFD capabilities in CONTAM 3 . 0 department of building , civil and environmental engineering, in: Concordia University , Canada Indoor Air Quality and Ventilation Group , Building and Fire Research Laboratory, National Institute of S, Fire Research, 2010, pp. 490–496.
[97] Tecplot Inc., Tecplot 360 Ex User's Manual, 2010, pp. 1–38.
[98] U.S. Environmental Protection Agency, U.S. EPA, Exposure Factors Handbook, 2011. EPA/600/R-.
[99] J. Westerweel, Fundamentals of digital particle image velocimetry, Meas. Sci. Technol. 8 (1997) 1379–1392, https://doi.org/10.1088/0957-0233/8/12/002.
[100] M. Raffel, C.E. Willert, F. Scarano, C.J. Kähler, S.T. Wereley, J. Kompenhans, Particle Image Velocimetry, third ed., Springer International Publishing AG, Cham, 2018 https://doi.org/10.1007/978-3-319-68852-7.
[101] J.B. Barlow, W.H. Rae, A. Pope, Low-Speed Wind Tunnel Testing, John Wiley & Sons, 1999.
[102] C.K. Choi, D.K. Kwon, Wind tunnel blockage effects on aerodynamic behavior of bluff body, Wind and Structures, Int. J. 1 (1998) 351–364, https://doi.org/10.12989/was.1998.1.4.351.
[103] W.D. Janssen, B. Blocken, H.J. van Wijhe, CFD simulations of wind loads on a container ship: validation and impact of geometrical simplifications, J. Wind Eng. Ind. Aerod. 166 (2017) 106–116, https://doi.org/10.1016/j.jweia.2017.03.015.
[104] B. Blocken, Computational Fluid Dynamics for urban physics: importance, scales, possibilities, limitations and ten tips and tricks towards accurate and reliable simulations, Build. Environ. 91 (2015) 219–245, https://doi.org/10.1016/j.buildenv.2015.02.015.
[105] D.A. Swanson, On the Relationship Among Values of the Same Summary Measure of Error when Used across Multiple Characteristics at the Same Point in Time: an Examination of MALPE and MAPE, 2015. https://escholarship.org/uc/item/1f71t3x9.
[106] J. Westerweel, F. Scarano, Universal outlier detection for PIV data, Exp. Fluid 39 (2005) 1096–1100, https://doi.org/10.1007/s00348-005-0016-6.
[107] A. Wood, R. Salib, CTBUH Technical Guide Natural Ventilation in High-Rise Office Buildings, 2013.
[108] Turkish Standards Institution, TS825 Thermal Insulation Requirements for Buildings, 825, 2009, p. 80.

[109] Z. Jin, X. Du, Y. Xu, Y. Deng, M. Liu, Y. Zhao, B. Zhang, X. Li, L. Zhang, C. Peng, Y. Duan, J. Yu, L. Wang, K. Yang, F. Liu, R. Jiang, X. Yang, T. You, X. Liu, X. Yang, F. Bai, H. Liu, X. Liu, L.W. Guddat, W. Xu, G. Xiao, C. Qin, Z. Shi, H. Jiang, Z. Rao, H. Yang, Structure of Mpro from SARS-CoV-2 and discovery of its inhibitors, Nature 582 (2020) 289–293, https://doi.org/10.1038/s41586-020-2223-y.
[110] N. Zhu, D. Zhang, W. Wang, X. Li, B. Yang, J. Song, X. Zhao, B. Huang, W. Shi, R. Lu, P. Niu, F. Zhan, X. Ma, D. Wang, W. Xu, G. Wu, G.F. Gao, W. Tan, A novel coronavirus from patients with pneumonia in China, 2019, N. Engl. J. Med. 382 (2020) 727–733, https://doi.org/10.1056/NEJMoa2001017.
[111] WHO, Transmission of SARS-CoV-2, Implications for Infection Prevention Precautions, 2020.